




Study of structural correlations with temperature dependent dielectric response and ferroelectric behavior for (Sr, Mn) co-doped BaTiO₃

Mehroosh Fatema¹, Akriti Bajpai¹, Anand Somvanshi¹, Samiya Manzoor¹, M. Arshad¹, Naima Zarrin¹, Aref A. A. Qahtan¹, Wasi Khan¹, and Shahid Husain^{1,*} 

¹Department of Physics, Aligarh Muslim University, Aligarh 202002, India

Received: 12 November 2021

Accepted: 18 January 2022

Published online:

31 January 2022

© The Author(s), under exclusive licence to Springer Science+Business Media, LLC, part of Springer Nature 2022

ABSTRACT

The present study reveals the effect of (Sr, Mn) co-doping on structural, dielectric, ferroelectric and electronic transport properties of Ba_{1-x}Sr_xTi_{1-x}Mn_xO₃ ($x = 0.0, 0.1$), synthesized by the solid-state reaction route. Rietveld refinement technique ensures mono-phase nature with tetragonal crystal structure and $P4mm$ space group. The variation in structural parameters highlights a distortion in the tetragonal phase instigated upon (Sr, Mn) co-doping. FTIR analysis reveals absorption bands in the region of 520–560 cm⁻¹ and 425–435 cm⁻¹ corresponding to Ti–O stretching (ν_1) and bending vibrations (ν_2), respectively, confirming the formation of TiO₆ octahedron. As estimated from the SEM micrographs, the grain sizes were found to fall in the range of 0.2–1.4 μm . The room temperature dielectric measurements reveal high value of dielectric constant for pristine sample ($\epsilon_r = 1121$), which decreases slightly upon co-doping ($\epsilon_r = 1081$). The samples exhibit the universal dielectric response phenomena within the low frequency regime (42 Hz–50 kHz). The temperature dependent dielectric measurements exhibit a thermally activated peak near 400 K for the pristine sample, which shifts towards lower temperatures for the doped sample, indicating a decrease in the Curie temperature. The conduction mechanism in this system is governed by the correlated barrier hopping model. The ac conductivity data have been used to estimate the binding energies (W_m) of the polarons and activation energy in different temperature regions. The room temperature ferroelectric hysteresis (P–E loops) studies reveal that the ferroelectricity in the system is suppressed under the effect of (Sr, Mn) co-doping. The negative temperature coefficient of resistivity (NTCR) characteristics indicate the semiconductor nature of these systems.

Address correspondence to E-mail: s.husaincmp@gmail.com

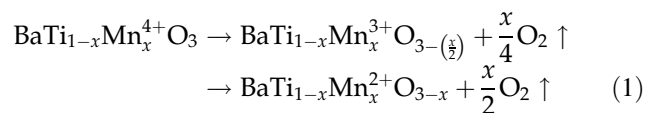
1 Introduction

Over the past decades, lead-free ferroelectric ceramics have gained wide attention owing to their non-toxic character and extraordinary electrical properties, which could be utilized in a variety of applications including ceramics capacitors, piezoelectric devices, thermistors and semiconductors [1, 2]. Barium titanate (BaTiO_3) is one of the most functional, and hence, extensively researched perovskite material on account of its exorbitant room temperature dielectric permittivity and ferroelectric behaviour [3–5]. Its properties such as dielectric and polarization response, conductivity mechanism and Curie temperature can be modulated by the chemical substitution of suitable dopants at the lattice sites to adhere to the robust demands for designing various electro-ceramic components [6, 7].

BaTiO_3 embraces a tetragonal perovskite structure at temperatures ranging from 7 °C to almost 130 °C [8–10]. Its Curie temperature is in the vicinity of 130 °C, beyond which it transforms to the cubic, paraelectric state [11]. Pristine BaTiO_3 is electrically insulating at room temperature and its dielectric characteristics are highly dependent on the synthesis process, density, grain size and sintering temperature. Several donor and acceptor impurities have been interminably explored for their impact upon the electrical properties via partial substitution of either Ba^{2+} ions (A-site doping) or Ti^{4+} ions (B-site doping) in BaTiO_3 (BTO) crystal lattice. The incorporation of divalent cations such as Ca^{2+} , Cu^{2+} and Sr^{2+} [12] and trivalent cations such as La^{3+} , Nd^{3+} , Dy^{3+} , Eu^{3+} , Ce^{3+} , Ho^{3+} , Eu^{3+} , also known as the magic dopants have been well explored and have been found to improve the lifetime of the capacitor [13–17]. Similarly, there are various accounts of divalent (Mn^{2+} , Ni^{2+}), tetravalent (Te^{4+} , Ce^{4+} , Zr^{4+} , Sn^{4+}) and pentavalent (Nb^{5+} , Sb^{5+} , Ta^{5+}) ion substitution at the Ti site, which reportedly promoted greater stability and enhanced optical, magnetic and thermal properties of the ceramics [7, 18, 19]. In particular, the substitution of Sr^{2+} in place of Ba^{2+} formed a solid solution of barium strontium titanate, which was very effective in modifying the physical parameters associated with BTO. Ortiz et al. [20] studied the impact of ball-milled Sr doped BaTiO_3 (0.01 mol% to 0.1 mol%) and obtained fine, dense microstructure within the 0.1 mol% sample, which displayed the highest relative density of over 99% of the theoretical value. The

tetragonal to cubic phase transition temperature was favourably tuned by varying the ratio of Sr/Ba to the room temperature range. Chamekh et al. [21] reported the synthesis of $\text{Ba}_{1-x}\text{Sr}_x\text{TiO}_3$ ($x = 0.0, 0.1, 0.2$) and proposed that these materials might be a potential candidate to be used as pyroelectrics, owing to their tunable Curie temperature. Their electrical impedance study established that the inhomogeneity of grains was minimum for 0.1 mol% Sr substituted BaTiO_3 . Moreover, it displayed both NTCR and PTCR effects upon varying the temperature.

Correspondingly, the impact of B-site substitution of Mn in BaTiO_3 is unique and has been receiving increasing attention in recent years. In BaTiO_3 ceramics, Mn is substituted at the octahedral Ti site on account of the smaller ionic radii of Mn^{2+} , Mn^{3+} and Mn^{4+} valence states, which transform during the sintering process given by the following reaction [4, 22]:



The concentration of oxygen vacancies changes upon the incorporation of Mn into BaTiO_3 and depending upon the valency of Mn, hence improving the conductivity of the material and reducing its permittivity. It has been reported that doping with Mn significantly reduced the Curie temperature of BaTiO_3 , and at the same time, increased the dielectric losses [23, 24]. Zhu et al. [25] have reported that manganese doped perovskites exhibit uniform microstructures accompanied, with unique multiferroic properties which could be utilized for future magnetic recording devices, ambient temperature sensors and spintronics. Dang et al. [26] have studied the crystal structure of $\text{BaTi}_{1-x}\text{Mn}_x\text{O}_3$ ($0 \leq x \leq 0.5$) by means of neutron powder diffraction and concluded that as the concentration of Mn dopant escalates, the system undergoes structural transformations from a polar tetragonal to hexagonal at $x > 0.09$ and further to a non-polar rhombohedral structure at $x > 0.12$. Along with the phase transformation, the 0.1 mol% Mn doped sample displays the smallest degree of distortion with the Mn–O bond length lying between 1.996 Å and 1.970 Å. A very high content of Mn dopant is found to deteriorate the performance of the ceramic capacitors which is attributed to the increase in oxygen vacancies and

associated imperfections [27]. The major consideration behind our decision to adopt Sr and Mn as co-dopants for BaTiO₃ was that the crystal structure of Mn doped BaTiO₃ readily transforms to hexagonal phase at room temperature [28, 29]. Sr²⁺ ions can suppress the formation of the hexagonal phase effectively and benefit the formation of single-phase tetragonal crystalline material [29–31]. Moreover, Sr²⁺ plays a key role in promoting a fine grained, dense microstructure with reduced heterogeneity in BaTiO₃ ceramics and is reported to lower the Curie temperature [20, 32]. These properties of Sr and Mn might be explored to make pyroelectric and multi-caloric devices [32, 33].

On reviewing the above-mentioned reports, we have found that the optimum values of the structural and electrical properties of BaTiO₃ were achieved at 0.1 mol% doping concentration of Sr and Mn independently at Ba and Ti sites, respectively. In the present study, detailed structural and electrical investigations of pristine and (Sr, Mn) co-doped BaTiO₃ ceramics have been accomplished, as Sr- and Mn-based ceramics might find applications at higher temperatures with variable frequencies. The variation in dielectric constant, ac conductivity and dc resistivity have been monitored over a wide range of frequencies and temperatures for the (Sr, Mn) co-doped samples. We have not found such studies on co-doped samples in the literature survey. Several analysis techniques have been utilized to ascertain the structural and control parameters such as Curie temperature, conduction mechanism, and the electronic transport mechanisms within the samples.

2 Experimental

2.1 Synthesis

Solid-state reaction route was employed to synthesize the BaTiO₃ and Ba_{0.9}Sr_{0.1}Ti_{0.9}Mn_{0.1}O₃ ceramics using AR grade chemicals Barium carbonate (BaCO₃), Titanium dioxide (TiO₂), Strontium Carbonate (SrCO₃) and Manganese Carbonate (MnCO₂) as initial precursors. The stoichiometric amounts were mixed in the acetone medium and sonicated for 40 min to aid homogenization. The solution was dried for 15 min under a hot lamp to evaporate most of the acetone and then the dried mixture was ground for 4 h using an agate mortar and pestle. During the

process of grinding, initially a paste is formed which gradually dries up as the acetone volatilizes and gets evaporated thoroughly. This mixture is then heated at 200 °C for 3 h in the furnace, followed by grinding and finally sintered at 900 °C for 3 h to get the desired phase of pristine and doped BaTiO₃. The samples have been synthesized at a lower sintering temperature as compared to earlier reported values, possibly due to ultrasonication.

2.2 Characterization

In order to analyze the structure and phase purity, the synthesized ceramic materials were characterized by powder x-ray diffraction (XRD) technique using a LabX XRD-6100 advanced X-ray diffractometer (Shimadzu-Japan) with Cu-K_α ($\lambda = 1.54 \text{ \AA}$) radiation. The XRD spectra were recorded in the 2θ range of 20° to 80° with the scanning rate of 4°/min and step size of 0.02°. The XRD data were refined with the Rietveld refinement technique using FullProf software. Fourier transform infrared (FTIR) measurements were performed on a circular pallet, prepared from a mixture of sample and KBr in the weight ratio of 1:100. The vibrational spectra were recorded in the transmission mode using Bruker Tensor 37 spectrometer in the wavenumber range of 400–4000 cm⁻¹. The surface morphology and quantitative elemental composition of the powder samples were performed by scanning electron microscopy (SEM) and energy dispersive analysis of x-rays (EDAX) using a JEOL, JSM-6510LV microscope at 15 kV operating voltage. The temperature dependent dielectric measurements in the frequency range of 42 Hz–1 MHz were carried out using Hioki LCR meter. For dielectric measurements, circular pellets were prepared and coated with silver paste on both sides of the sintered pellets in order to obtain the parallel plate capacitor configuration. Room temperature ferroelectric characterization was performed through standard multiferroic PE loop tracer (Model: 20PME 1kHz 0.01 M, Marine, India) in which circular pellets were immersed in silicon oil to avoid sparking at high voltages. The variation of dc resistivity with temperature was carried out by two-probe method using SES electronics TPX-200C electrometer.

3 Results and discussions

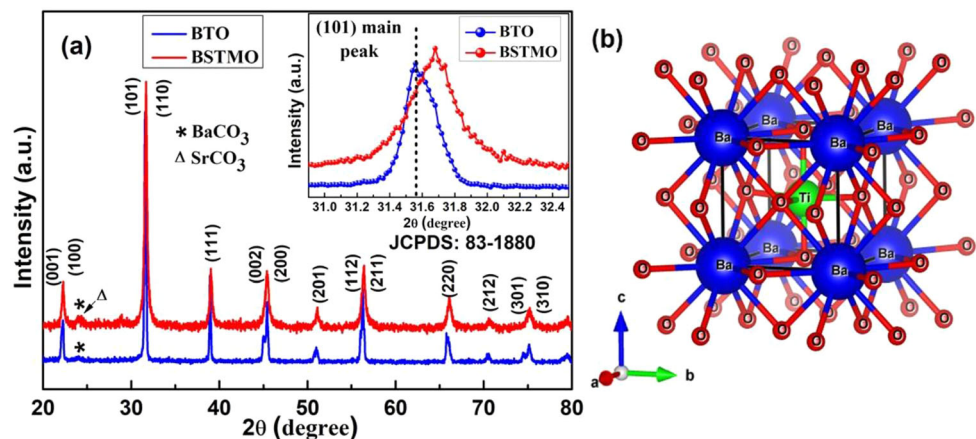
3.1 Structural analysis

The XRD patterns of BaTiO₃ (BTO) and Ba_{0.9}Sr_{0.1}Ti_{0.9}Mn_{0.1}O₃ (BSTMO) recorded at ambient temperature are shown in Fig. 1. The well-resolved peaks match thoroughly with the tetragonal crystal structure having *P4mm* space group (JCPDS#83-1880). The sharp and distinct diffraction peaks corresponding to the planes (001), (100), (101), (110), (111), (002), (200), (201), (112), (211), (220), (212), (301) and (310) confirm the formation of well crystallized single-phase polycrystalline BTO. With the introduction of Sr²⁺ at the A-site and Mn²⁺ at the B-site of the perovskite ABO₃, the double peaks at (001)–(100), (002)–(200), (112)–(211) and (301)–(310) merge, revealing the distortion in the tetragonal structure of BSTMO. It also signifies a reduction in the degree of crystallinity in the sample with the addition of the (Sr, Mn) dopants, along with the formation of crystal defects in the system [34]. A minor satellite peak is observed at $2\theta = 23.9^\circ$ in the pristine sample corresponding to BaCO₃ impurity (JCPDS 41-0373). With doping, the impurity peak becomes prominent due to the additional contribution from SrCO₃ compound. (JCPDS 05-0418). However, the intensity of the peaks remains almost negligible owing to the low doping concentration.

In order to obtain the detailed structural information of the samples, the XRD data have been fitted by the Rietveld refinement technique, using the Fullprof software. The diffraction data have been refined using the tetragonal structure and *P4mm* space group (Fig. 2). The peaks have been modelled in the *Pseudo-Voigt* shape profile, whereas the background has been defined by the 6- coefficient polynomial function.

This process has been systematically carried out beginning with the refinement of the scale, overall B factor and further proceeding to refining the atomic position parameters (*x*, *y*, *z*), lattice parameters, background and peak shape. The observed diffraction peaks of BSTMO exhibit the tetragonal perovskite structure (*P4mm*), similar to that of pristine BTO. The crystal structure of BTO obtained after refinement has been modelled using VESTA software [35] and is shown in Fig. 1b. The lattice parameters (*a*, *b*, *c*), tetragonality (*c/a*), Reliability factors (*R_p*, *R_{wp}*, *R_{exp}*), the goodness of fit parameters (χ^2), unit cell volume and density of the unit cell are given in Table 1. The lattice parameters, tetragonality and unit cell volume have been found to decrease for the doped sample. This decrease can be attributed to the lower effective ionic radii of Sr²⁺ (1.31 Å) as compared to that of Ba²⁺ (1.75 Å) cation. Manganese ions are reportedly present in multiple valence states irrespective of the starting precursor used due to thermal effects [4]. The ionic radii of the B-site ions have been reported as Ti⁴⁺ (0.605 Å), Mn⁴⁺ (0.53 Å), Mn³⁺ (0.645 Å) and Mn²⁺ (0.83 Å) [36]. Manganese, when doped in low concentrations, does not have significant impact on the crystallite size of the material, because the ionic radii of Mn in all its valence states are comparable to that of the Ti⁴⁺ ion. The substitution of dopants Sr²⁺ and Mn²⁺, having smaller ionic radii causes local distortion in the octahedral units, resulting in the decrease in unit cell volume, lattice parameters, bond lengths, bond angles and increase in the density of the crystal structure (Table 1). The slightly larger values of (*R_p*, *R_{wp}*, *R_{exp}*) are due to the low signal to noise ratio, but

Fig. 1 **a** Plots showing the XRD patterns of BTO and BSTMO samples. (Inset): Shift of most intense peak of the samples. **b** Crystal Structure of BaTiO₃ as visualized by VESTA software



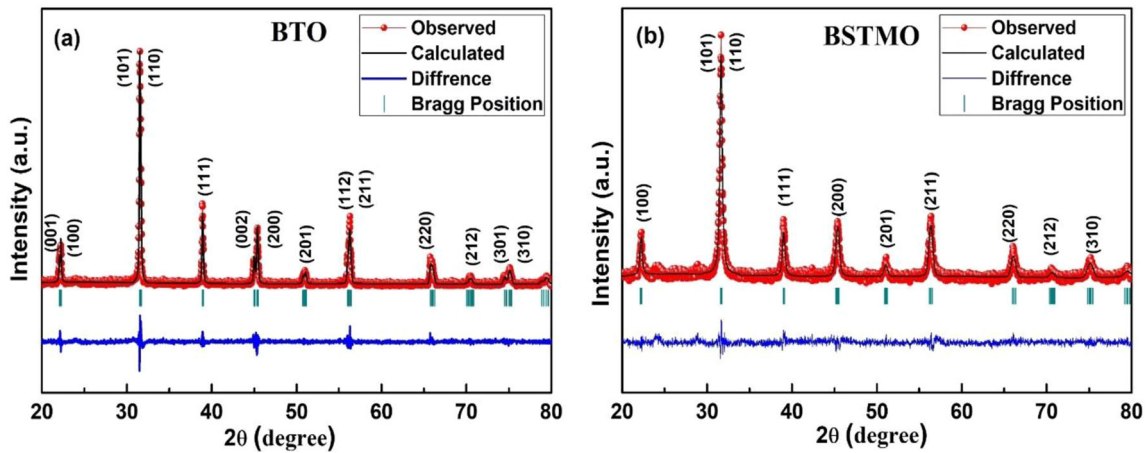


Fig. 2 Rietveld refined patterns of **a** pristine BTO and **b** BSTMO samples

Table 1 Structural parameters of BTO and BSTMO samples as estimated using Rietveld refinement analysis

| Structural parameters | | BTO | BSTMO |
|---------------------------|---|---------------------------------|--------------|
| Crystal family | | Tetragonal | Tetragonal |
| Space group | | P4mm | P4mm |
| Profile fitting functions | | Pseudo-Voigt | Pseudo-Voigt |
| Lattice parameters | | | |
| | <i>a</i> (Å) | 3.9968 | 3.9917 |
| | <i>b</i> (Å) | 3.9968 | 3.9917 |
| | <i>c</i> (Å) | 4.0277 | 4.0119 |
| Tetragonality | | (<i>c/a</i>) | 1.0077 |
| Unit cell volume | | <i>V</i> (Å ³) | 64.34 |
| Goodness of fitting | | (χ^2) | 1.61 |
| Reliability-factors (%) | | | |
| | <i>R_p</i> | 10.4 | 10.5 |
| | <i>R_{wp}</i> | 13.0 | 13.6 |
| | <i>R_{exp}</i> | 10.25 | 11.83 |
| Bragg-R factors (%) | | | |
| | <i>R_B</i> | 5.62 | 6.89 |
| | <i>R_f</i> | 5.33 | 5.82 |
| Density | | ρ (gm/cm ⁻³) | 6.15 |
| Bond angle | | Ti–O _i –Ti (degree) | 174.55 |
| Bond length | | Ba/Sr _i –O (avg) (Å) | 2.82 |
| | Ti/Mn _i –O _I (Å) | 2.27 | 2.27 |
| | Ti/Mn _i –O _{II} (Å) | 2.00 | 1.99 |

the low values of goodness of fit parameter (χ^2), justifies the precision of the refinement.

Goldschmidt’s tolerance factor (τ) has been calculated to measure the stability of the perovskite crystal structure and to quantify the extent of distortion introduced upon (Sr, Mn) co-doping in BaTiO₃ [37]. Its value is ascertained by the formula:

$$\tau = \frac{r_{Ba/Sr} + r_O}{\sqrt{2}(r_{Ti/Mn} + r_O)} \quad (2)$$

where $r_{Ba/Sr}$ and $r_{Ti/Mn}$ represent the average ionic radii of cations at A and B sites of ABO₃ perovskite, respectively, whereas r_O is the radius of the anion

(Oxygen). The colossal difference in the ionic radii of Ba²⁺ and Ti⁴⁺ leads to the high value of tolerance factor, τ , which amounts to 1.07. Its value reduces to 1.06 upon 10 mol % doping of Sr and Mn ions, as Sr²⁺ significantly lowers the average ionic radii of A-site cation from 1.75 Å to 1.70 Å, hence reducing the difference between the radii of A and B cations. The reduction in the tolerance factor indicates a distortion produced in the crystal structure and validates the results obtained from the Rietveld analysis. The value of $\tau > 1$ signifies that the pristine and codoped samples belong to the tetragonal crystal family [38].

The crystallite size (D) has been calculated by the Scherrer's equation [39] which is represented as

$$D = \frac{k\lambda}{\beta \cos \theta} \quad (3)$$

where β is the full width at half maximum (FWHM), θ is the Bragg angle, k is dimensionless constant and represents the shape factor (0.9) and λ indicates wavelength of Cu- k_α radiation (1.54 Å). Here, β originates from the finite grain size of the crystalline material. The crystallite size of BTO has been found to be 39.7 nm which decreases to 23.6 nm for the doped sample. This is confirmed by the broadening of the peaks for the doped sample, that indicates greater FWHM values. Figure 1a (inset) shows that the diffraction peaks also exhibit a shift towards the higher diffraction angles which is in accordance with the Bragg law [40]. It indicates a decrease in the interplanar spacing of the doped sample, leading to greater unit cell density, lower values of unit cell volume, lattice parameters, bond angle and bond lengths in case of BSTMO specimen.

3.2 Williamson–Hall analysis

Crystallite size has also been calculated using the Williamson–Hall approach [41–43], which states that the line broadening observed in the XRD spectra may be arising because of two mutually independent factors. The width of the Bragg peak consolidates instrument and material dependent modifications. The instrument corrected broadening β_D , is consistent with the diffraction peak of the samples, and is approximated by the relation:

$$\beta_D^2 = (\beta_{\text{measured}}^2 - \beta_{\text{instrumental}}^2) \quad (4)$$

On substituting the value of β_D from Eq. (4) to Eq. (3), we get the Scherrer's equation as

$$D = \frac{k\lambda}{\beta_D \cos \theta} \quad (5)$$

The Williamson–Hall analysis also incorporates the strain-induced broadening β_S , arising from crystal distortion, defects, and presence of imperfections, which is given by the Wilson Formula [44], $\beta_S = 4\epsilon \tan \theta$.

Based upon the assumption that these two broadening contributions are mutually independent, the total reflection width is estimated by replacing β of

Eq. (5) with, $\beta_{\text{hkl}} = \beta_S + \beta_D$, hence transforming to the final equation:

$$\beta_{\text{hkl}} = \left(\frac{k\lambda}{D \cos \theta} \right) + 4\epsilon \tan \theta \quad (6)$$

The term $(k\lambda/D \cos \theta)$ represents the size broadening whereas, $4\epsilon \tan \theta$ depicts the microstrain broadening.

Multiplying both sides of Eq. (6) with $\cos \theta$, we obtain the relation:

$$\beta_{\text{hkl}} \cos \theta = \left(\frac{k\lambda}{D} \right) + 4\epsilon \sin \theta \quad (7)$$

Table 2 lists the values of 2θ , broadening β , along with the hkl values of selected peaks for Williamson–Hall analysis. The slope of $\beta \cos \theta$ versus $4\sin \theta$ plot (Fig. 3) gives the lattice strain and the intercept is used to calculate the crystallite size, as summarised in Table 3. Equation (7) is acknowledged as uniform deformation model (UDM) for Williamson–Hall Analysis. In this model, the strain is assumed to be uniform in all crystallographic directions, hence considering the isotropic nature of the crystal [45].

3.3 Fourier transform infrared (FTIR) spectroscopy

The Fourier transform infrared (FTIR) spectra of BTO and BSTMO samples have been recorded in the transmission mode, as shown in Fig. 4a. The FTIR absorption spectra are sensitive to the formation of the chemical bonds and depict the different functional groups and vibrational modes present in the samples. The information related to the interaction of the atomic and molecular forces within the crystal lattice can be extracted by this technique. The energy

Table 2 Peak broadening (β) and 2θ values, with corresponding Miller indices of peaks used in Williamson–Hall analysis

| Miller indices hkl | BTO | | BSTMO | |
|----------------------|------------------------|----------------------|------------------------|----------------------|
| | 2θ (degrees) | β (degrees) | 2θ (degrees) | β (degrees) |
| (100) | 22.20 | 0.252 | 22.27 | 0.322 |
| (101) | 31.59 | 0.202 | 31.67 | 0.343 |
| (111) | 38.95 | 0.155 | 39.05 | 0.321 |
| (200) | 45.32 | 0.455 | 45.39 | 0.478 |
| (201) | 50.99 | 0.385 | 51.09 | 0.346 |
| (211) | 56.27 | 0.331 | 56.39 | 0.455 |
| (220) | 65.93 | 0.373 | 66.11 | 0.448 |

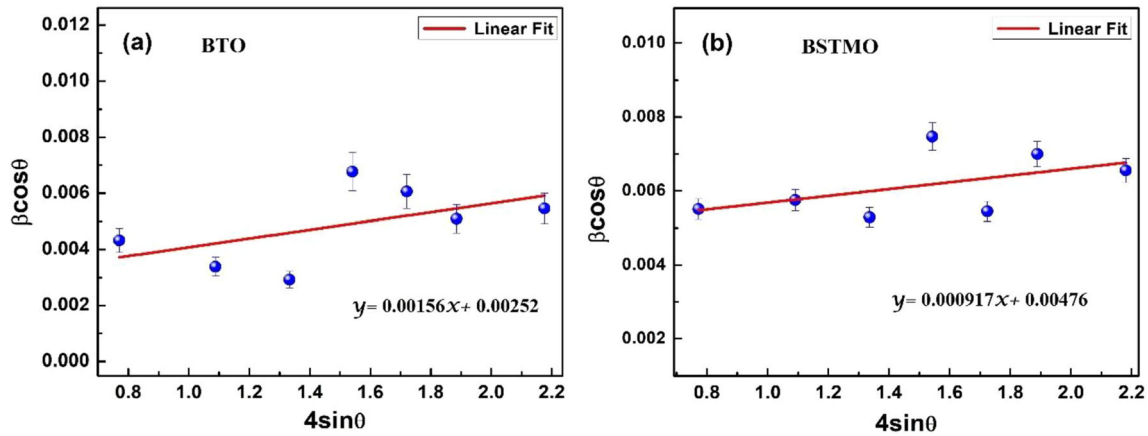
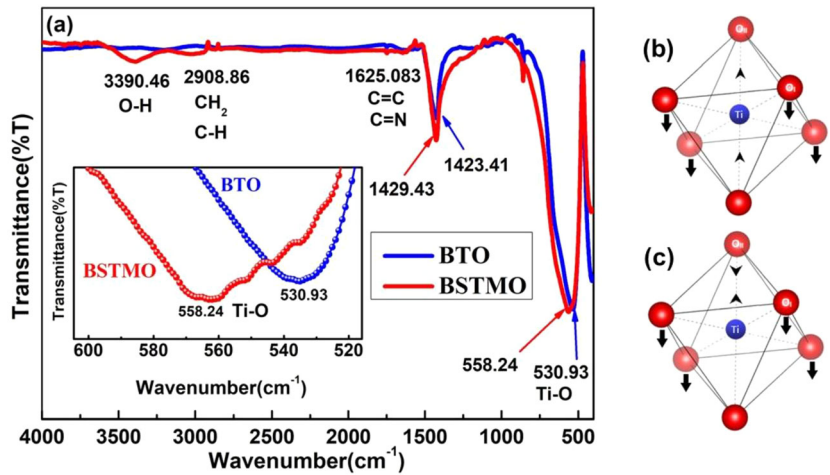


Fig. 3 Williamson-Hall plots of BTO and BSTMO using UDM (uniform deformation model)

Table 3 Crystallite Size, Lattice strain, Grain size and Tolerance factor of BTO and BSTMO samples

| Samples | Crystallite size (nm) | | Lattice strain (η) | Grain size (μm) (from SEM) | Tolerance factor (τ) |
|---------|-----------------------|------------------------|---------------------------|--|-----------------------------|
| | Scherrer's equation | Williamson-Hall method | | | |
| BTO | 39.7 | 55.0 | 1.56×10^{-3} | 1.05 | 1.07 |
| BSTMO | 23.6 | 29.1 | 9.2×10^{-4} | 0.68 | 1.06 |

Fig. 4 a FTIR spectra of BTO and BSTMO samples
 b Bending and
 c Stretching Vibrations of Ti-O bond.



of the molecule influences the position of the absorption peaks in the FTIR spectra. Molecules having greater energy occupy the position with higher wavenumber.

The vibrational bands present in the region 520–560 cm^{-1} is the characteristic band of metal-oxide Ti-O stretching vibration in the TiO_6 octahedron and confirm the formation of BaTiO_3 [46]. The low frequency absorption band near 428 cm^{-1} corresponds to the Ti-O_{II} bending vibration [9, 47].

Figure 4b, c depicts the bending and stretching vibrations of TiO_6 octahedra. The absorption bands at 860 cm^{-1} and 1197 cm^{-1} are due to the C-H bending modes of ethanol. The band at 1420 cm^{-1} appears due to the symmetric stretching vibrations of the carboxylic group, instigated by the barium carbonate precursor. The bands in the vicinity of 1550 cm^{-1} indicate the presence of C=C bending and C=N stretching mode [48]. The characteristic absorption bands near 1625 cm^{-1} are attributed to the O-H

bending modes of ethanol. The band between 2900 cm^{-1} and 3100 cm^{-1} corresponds to the C–H stretching vibration and confirms the presence of functional groups CH_2 and CH_3 . The characteristic absorption band near 3390 cm^{-1} is due to the presence of O–H stretching vibration of H_2O and indicates the presence of moisture in the sample [49].

The average Ti/Mn–O bond length (r) can be estimated by the following relation [50, 51]

$$r = \left(\frac{17}{k}\right)^{1/3} \quad (8)$$

where k is the average force constant of Ti/Mn–O bond. The value of k has been derived from Hook's law, which relates the transmission wave number ($\bar{\nu}$) of stretching vibration to the force constant and reduced mass of the molecular system as,

$$\bar{\nu} = \left(\frac{1}{2\pi c}\right) \sqrt{\frac{k}{\mu}} \quad (9)$$

where $\bar{\nu}$ represents the wavenumber in cm^{-1} , c is the speed of light, μ denotes the effective mass of the sample which is given by,

$$\mu = \frac{M_{\text{O}} \times [xM_{\text{Mn}} + (1-x)M_{\text{Ti}}]}{M_{\text{O}} + [xM_{\text{Mn}} + (1-x)M_{\text{Ti}}]} \quad (10)$$

Here, M_{O} , M_{Mn} and M_{Ti} represent the atomic weights of O, Mn and Ti ions, respectively, and x is proportion of Mn with respect to Ti within BTO. Hence the quantities k , μ and r of the samples can be estimated using the above equations and their values have been summarised in Table 4.

The Ti–O bond length decreases with the inclusion of Mn atoms at the Ti site, while the force constant increases. This change in the vibrational bonds is evident from the metal-oxide band shift towards the higher wavenumber. The inset image of Fig. 4a shows a shift in the Ti–O peak from 530.93 to 558.24 cm^{-1} , with the incorporation of the Sr^{2+} and Mn^{2+} dopants in the BSTMO sample. This peak shift

towards higher wavenumber is attributed to the lower effective ionic radii of Sr^{2+} (1.31 \AA) as compared to that of Ba^{2+} (1.75 \AA) cation. The substitution of the dopants, having smaller ionic radii causes a decrease in unit cell volume, leading to an increase in the bond dissociation energy of the doped sample [9, 49]. This deformation in crystal structure leads to an increase in the force constant of the vibrating bond of the doped sample, which results in spectral variation. This observation is in close agreement with the results obtained from the XRD analysis.

3.4 Morphological studies (SEM and EDAX)

The microstructure of the BTO and BSTMO samples has been probed using a scanning electron microscope (SEM) combined with an energy dispersive analysis of x-rays (EDAX) to estimate the elemental composition. The recorded SEM micrographs for pristine and doped BTO samples are shown in Fig. 5. The micrograph analysis of BTO reveals micro-sized particles with considerable variation in the particle size [Fig. 5a, b]. The microstructure of the doped sample [Fig. 5c, d], reveals irregular particle shapes and macro-agglomerations with decreased grain size. The microstructure of the BTO exhibits large rectangular crystals with substantial porosity, which may be due to the gases released during calcination at $900\text{ }^\circ\text{C}$. The grain size of the BSTMO is reduced upon Sr and Mn substitution which is in accordance with XRD studies. The reduction in the particle size can be attributed to the enhanced nucleation sites. Incorporation of Mn induces charge imbalance, promotes the creation of oxygen vacancies and causes structural distortion which leads to the decrease in the crystallinity of the samples. The decrease in the crystallinity is evident from the micrographs. The high porosity of the pristine sample is also reflected in the temperature dependent resistivity studies [52].

Table 4 Transmission wave number ($\bar{\nu}$), Force constant (k), effective mass (μ), bond length (r) of BTO and BSTMO samples as obtained from FTIR spectra and Rietveld Refinement

| Sample | $\bar{\nu}$ (cm^{-1}) (Ti/Mn–O) From FTIR | k (N/cm) | μ (amu) | r (\AA) (Ti/Mn–O) From FTIR | r (\AA) (Ti/Mn–O) From Rietveld Refinement |
|--------|--|------------|-------------|--|---|
| BTO | 530.93 | 2.00 | 11.99 | 2.03 | 2.00 |
| BSTMO | 558.24 | 2.22 | 12.03 | 2.00 | 1.99 |

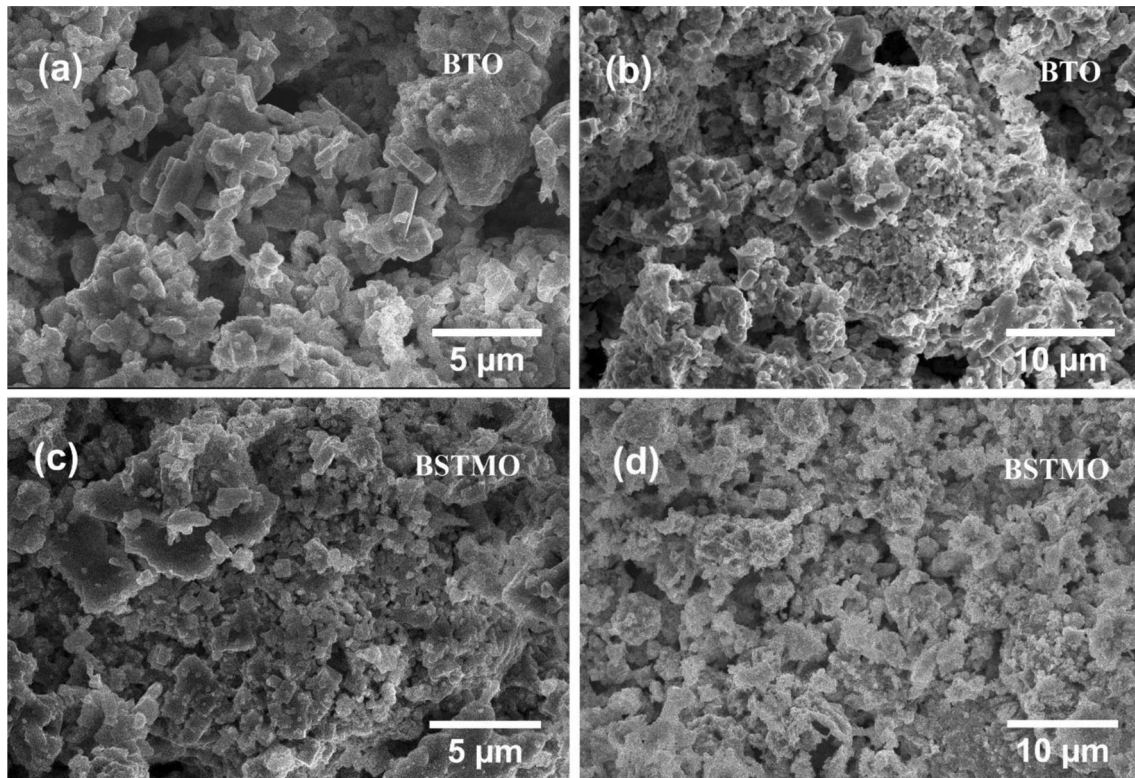


Fig. 5 a–d SEM micrographs of BTO and BSTMO at 5 μm and 10 μm scales

Figure 6 shows the grain size distribution of BTO and BSTMO samples which lies in the range of 0.2–1.4 μm . The grain size of doped ceramics manifests micro-scaled, small and narrow distribution. The average grain size decreases from 1.05 μm for BTO to 0.68 μm for BSTMO sample. The large grain size in the pristine sample may be due to the non-uniform dissemination of the oxide precursors in the lattice.

The EDAX spectra of the constituent elements recorded in the energy range of 0–20 keV are

presented in Fig. 7. The peaks appearing in the EDAX patterns are that of the constituent elements (Ba, Ti, O, Sr and Mn) only. This confirms that there is no impurity present in the synthesized samples. Inset data of Fig. 7 validate the integration of Mn at Ti site and Sr at Ba site. The relative substitution of the dopant elements at the A and B sites of the perovskites is in the vicinity of the expected concentration.

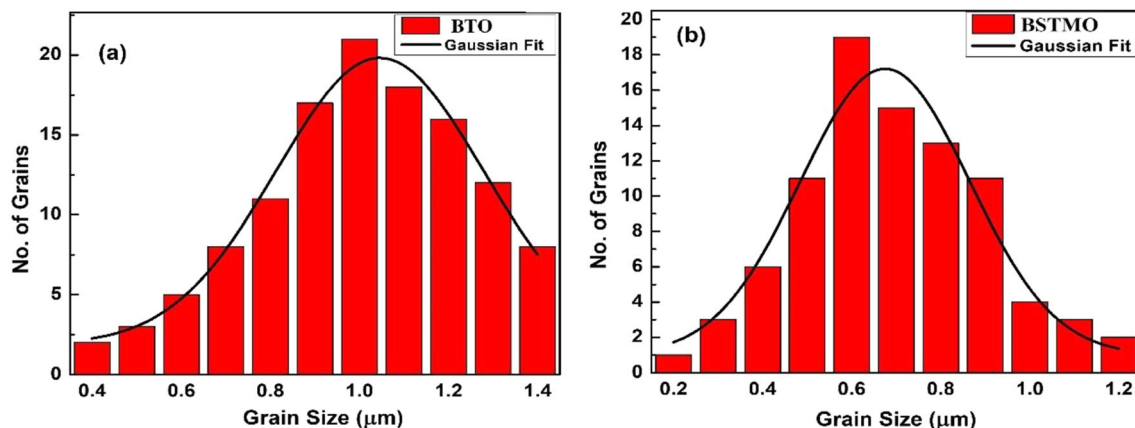


Fig. 6 Histograms obtained from grain size distribution analysis of SEM micrographs of **a** BTO, and **b** BSTMO samples along with their Gaussian fit

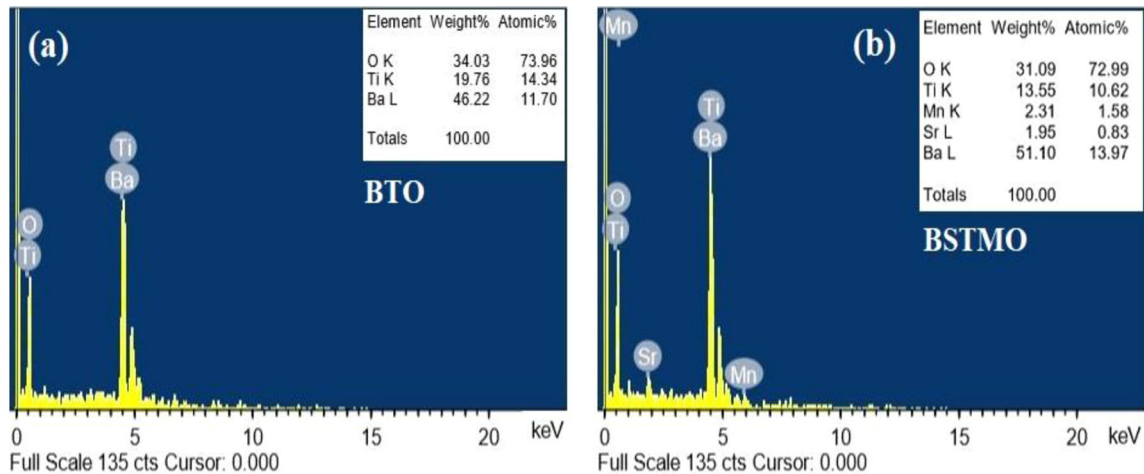


Fig. 7 EDAX spectra of **a** BTO and **b** BSTMO samples

3.5 Dielectric analysis

In the field of dielectrics, BaTiO_3 holds one of the most prestigious positions owing to its very high dielectric permittivity, which makes it a potential candidate for highly efficient capacitors. Dielectric properties of BTO and BSTMO ceramics (dielectric permittivity (ϵ_r) and dissipation factor ($\tan\delta$)) have been investigated as a function of frequency and temperature. The complex permittivity is the parameter of prime importance in the dielectric analysis and is given by Eq. (11)

$$\epsilon^*(\omega) = \epsilon'(\omega) - i\epsilon''(\omega) \quad (11)$$

Here $\epsilon'(\omega)$ represents the real part of the entity $\epsilon^*(\omega)$ and defines the energy storage capability of the material, whereas the imaginary part $\epsilon''(\omega)$ represents the energy dissipation in the form of heat within the ceramics. The real part of the dielectric permittivity has been obtained from the experimentally measured values of the capacitance by the relation

$$\epsilon' = \frac{C_p d}{\epsilon_0 A} \quad (12)$$

Here C_p , d and A denote the capacitance, thickness and cross-sectional area of the circular pellet, respectively, and $\epsilon_0 = 8.854 \times 10^{-12}$ F/m is the permittivity of the free space.

Dielectric properties of pristine and doped BaTiO_3 ceramics have been investigated in the frequency range of 42 Hz to 50 kHz at room temperature (Fig. 8a). The samples exhibit very high values of dielectric constant at lower frequencies, their highest values being 1121 and 1081 for pristine and doped

samples, respectively. The samples exhibit distinct dispersive behaviour for the entire frequency range. The sharp decline in dielectric constant with frequency is attributed to the lower contribution from ionic and dipolar polarizations and as well as space charge polarization. This may also be due to the creation of the crystal imperfections such as defects, voids, oxygen vacancies and the additional effects pertaining to the substitution of Sr^{2+} and Mn^{2+} ions in pristine BTO. The dielectric constant subsequently attains an almost constant value at a frequency greater than 5 kHz. It can be explained on the basis of Maxwell–Wagner type of interfacial polarization effect [53]. In the low frequency region, the electric dipoles effortlessly follow the polarity alteration of applied ac field and orient themselves accordingly. At higher frequencies, the polarity of ac field undergoes a rapid change. Some of the dipoles are not competent enough to follow this change and leading to a decrease in the values of $\epsilon'(\omega)$. In the high frequency region, ionic and orientational polarizations do not contribute to the dielectric constant and only electronic polarization gives rise to $\epsilon'(\omega)$. The drop in the values of the dielectric constant of the doped sample corresponds to the smaller crystallite size as well as the diminished grain size and increased density of the microstructures. As evident from the Rietveld refinement data, the tetragonality (c/a) has reduced for the BSTMO samples due to incorporation of Sr^{2+} ion. Reduction in tetragonality implies that the structure is closer to the cubic configuration, which is more symmetric, leading to a decreased dielectric constant [54].

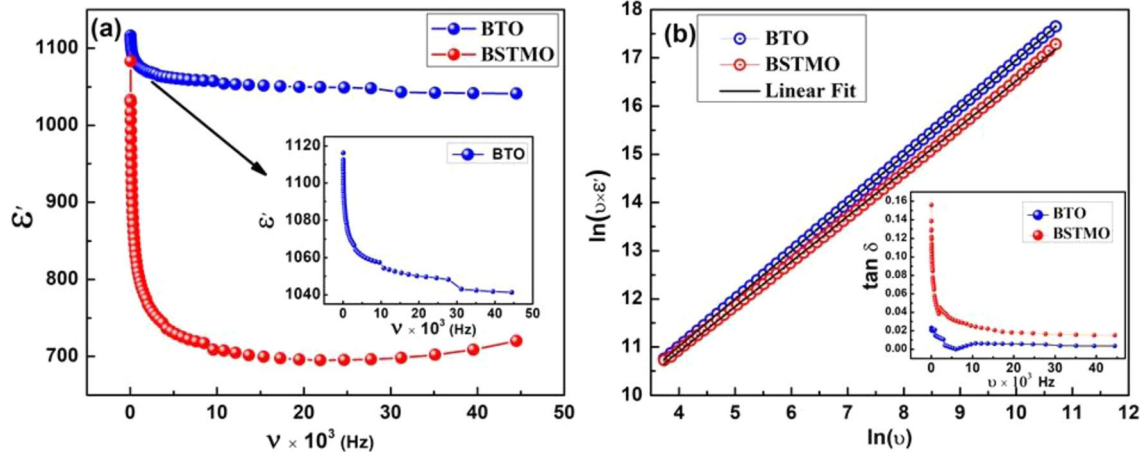


Fig. 8 a Plots of real part of dielectric permittivity against frequency of applied field for BTO and BSTMO samples. Inset in the figure represents the enlarged view for BTO sample. **b**

The behaviour of the frequency dependent dielectric response has been studied through the universal dielectric response (UDR) model. According to this model, the hopping of localized charge carriers between spatially fluctuating lattice potentials not only generate conductivity but also instigates the dipolar effects. Mathematically, ϵ' is given by

$$\epsilon' = \frac{\tan\left(\frac{s\pi}{2}\right)\sigma_0}{\epsilon_0} f^{\alpha-1} \quad (13)$$

where, σ_0 and s depict the temperature dependent constants and f is the frequency. Rearranging Eq. (13) gives,

$$f \times \epsilon' = A(T) \times f^\alpha \quad (14)$$

where $A(T) = \tan(s\pi/2)\sigma_0/\epsilon_0$ is a temperature dependent constant. The above relation (14) holds if the plot of $\log(f\epsilon')$ versus $\log(f)$ follows a straight line trajectory, whose slope is equal to ' α '. This inference was justified from the linear plots in Fig. 8b. The samples exhibit linear behaviour in the entire frequency range, implying that the UDR model is accountable for the dielectric response within these samples at all the probing frequencies.

Inset of Fig. 8b denotes the frequency dependence of dielectric loss factor ($\tan\delta$) of BTO and BSTMO at room temperature. Both the samples display the higher value of $\tan\delta$ in the low frequency region due to the losses associated with the dielectric lagging. Further, the space charge polarization induced upon the capture of surface electrons by the impurities and defects present in the crystal lattice, also contributes

$\ln(\nu \times \epsilon')$ versus $\ln(\nu)$ plots to depict the UDR behavior of the BTO and BSTMO samples. Inset represents the tangent losses as a function of frequency of the applied field

towards the higher losses. Due to the trapped electrons, more energy is required for their motion, leading to migration losses. The decrease of tangent loss at higher frequencies may be attributed to the reduction in interfacial polarization. In this region, the dielectric constant depends only on the hopping of electrons. Dielectric loss signifies energy dissipation in the material. It corresponds to the lost applied electrical field energy as thermal energy, and thereby heating up the system. Sr and Mn are responsible for an increment in the dielectric loss of the sample, which has also been reported in previous studies [55].

Figure 9a–d shows the dielectric constant of BTO and BSTMO samples as a function of temperature at specified frequencies. In case of both the samples, the dielectric constant increases with the rise in temperature, and exhibit an anomaly in the temperature range of 370–410 K, corresponding to the Curie temperature. The structure of BTO undergoes a phase transformation from tetragonal to cubic at around 400 K, whereas BSTMO transforms at a relatively lower temperature, near about 380 K. The dielectric permittivity shows a slight decline in this region because some of the thermal energy is utilized in the re-orientation of the domains resulting in loss of ferroelectricity and acquisition of paraelectric state. With further increase in temperature the polarisation is enhanced due to increased polaron hopping. Moreover, the thermal expansion of the lattice stimulates the mobility of bound charge carriers which are present at the defect sites within the samples. These bound charges align themselves according to

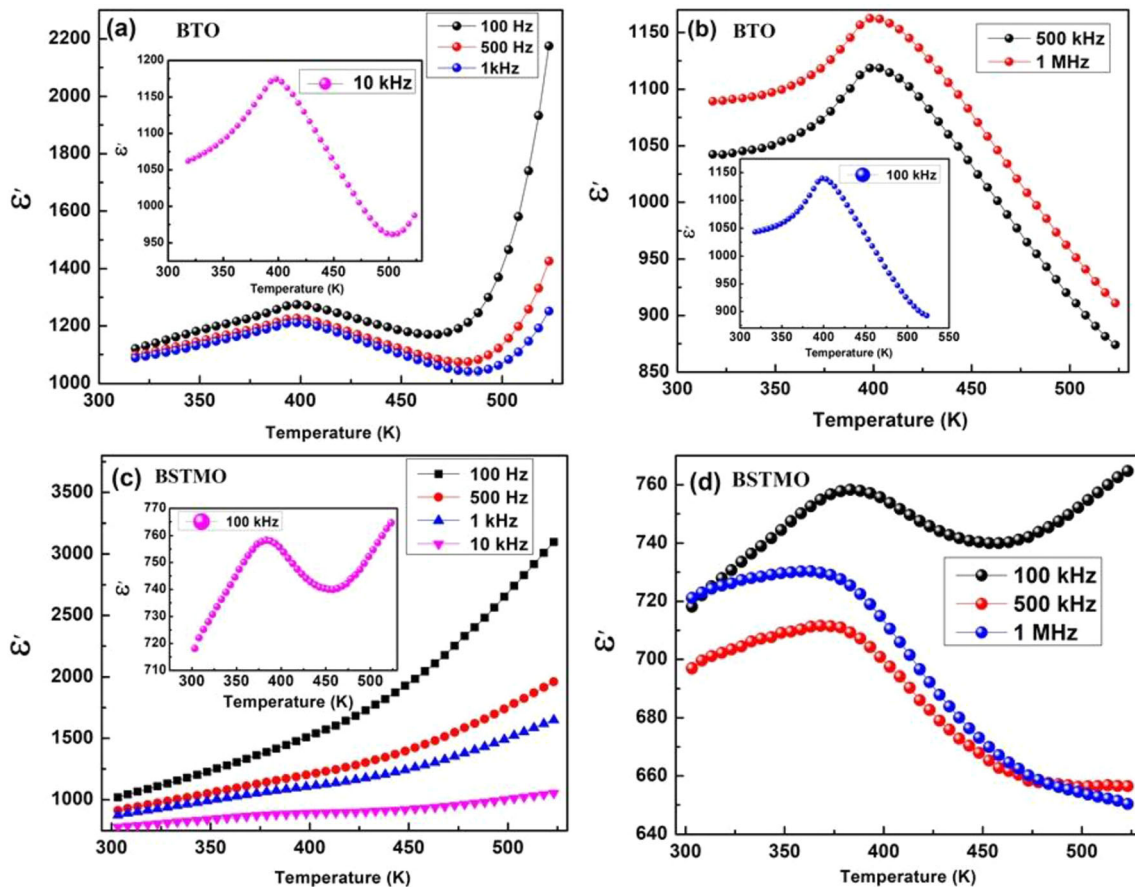


Fig. 9 a–d Plots of dielectric constant as a function of temperature at selected frequencies for BTO and BSTMO

the applied electric field, hence increasing the polarisation. However, for higher values of frequencies (Fig. 9b, d), the permittivity reduces in accordance with the Maxwell–Wagner polarisation effect. It can be observed from Fig. 9d that BSTMO ceramic has broad peaks, which denotes the diffused type transition, which is a characteristic disordered perovskite structure and it highlights that the tetragonal to cubic transformation is diffused. The results are consistent with the earlier reported observations [19].

The temperature dependence of dielectric loss of BTO and BSTMO at selected frequencies is shown in Fig. 10a, b. The dielectric loss is found to increase with the increase in temperature while it decreases with the increase in frequency. The temperature dependent enhancement in $\tan\delta$ may be attributed to the generation of impurities and defects and also due to dipole vibrational losses leading to fatigue in the system. Both Mn and Sr lead to an upsurge of doubly ionized oxygen vacancies at elevated temperature, which can be explained by Kröger–Vink notation:



The increase in the oxygen vacancies leads to enhanced conduction losses in the doped sample. Dielectric loss is directly proportional to the ac conductivity in the medium and correspondingly increases with the increment in temperature. This may be attributed to the migration of the ions during which they impart their energies to the lattice. The appearance of the peak at around 380–420 K confirms the relaxor type behaviour in the BTO sample.

Cole–Cole analysis has been executed to examine relaxational behaviour for these samples. Figure 11 shows the Cole–Cole plots for BTO and BSTMO specimen at room temperature, which is constructed by plotting the imaginary part of the dielectric permittivity ($\epsilon'' = \epsilon' \tan\delta$) against its real part (ϵ'). The variation of ϵ'' with ϵ' does not follow a semi-circular trajectory, rather it exhibits a nearly linear behaviour at higher frequencies for both the samples. We did not observe any substantial impact of Sr and Mn

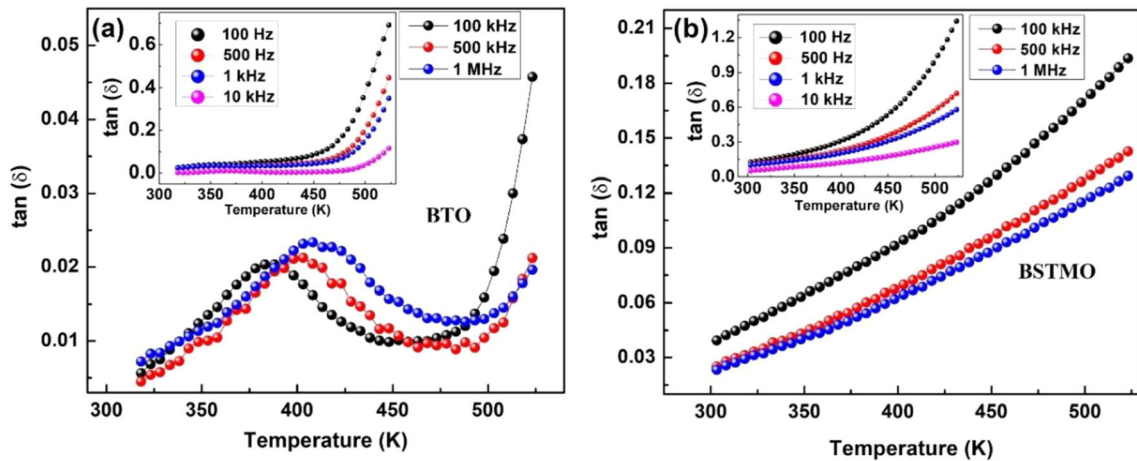


Fig. 10 Plots of $\tan \delta$ as a function of temperature at selected frequencies for a BTO and b BSTMO samples

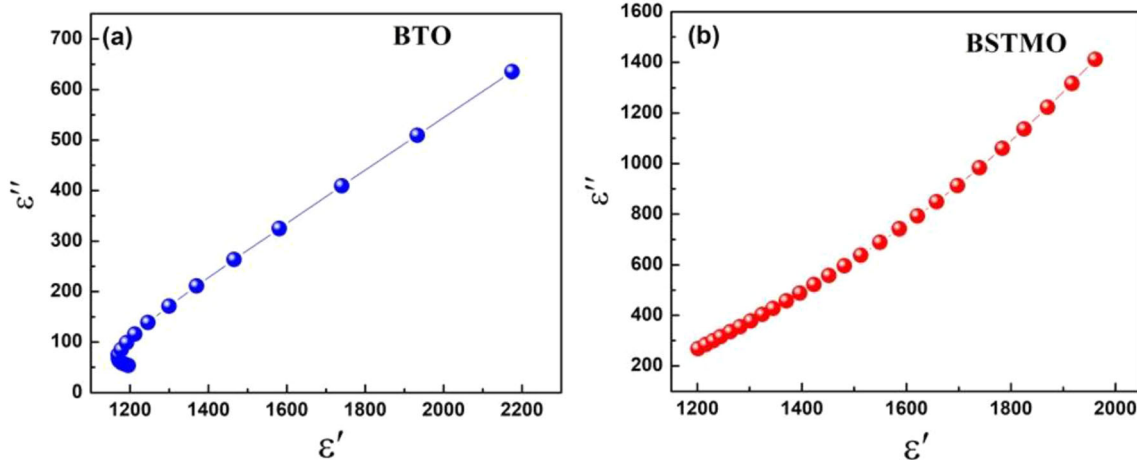


Fig. 11 Cole–Cole plots for a BTO and b BSTMO

substitution on the Cole–Cole profile, indicating that both the samples exhibit non-Debye type of relaxation in the applied frequency range at room temperature, which can be attributed to the inhomogeneity in the formation of grains and surface roughness [21]. The lower values of conductivity might also be responsible for the non-Debye behaviour of the samples. The presence of the tail in the low frequency region shows an almost mono-dispersive or narrow-ranging dispersal of the relaxation for electron hopping due to heavy losses in a specimen.

To conclude, the samples exhibit very high values of dielectric constant at lower frequencies, which sharply decreases with an increase in frequency, which is in accordance with the Maxwell–Wagner interfacial polarization effect. The slight decrease in highest value of dielectric constant is observed for

(Sr, Mn) co-doped sample which is consistent with the structural and morphological studies. Temperature dependent studies reveal that the samples obey the UDR model. Cole–Cole analysis reveals the existence of non-Debye type of relaxation in both the samples.

3.6 Conduction mechanism

Physical characteristics, such as dielectric permittivity, losses and conductivity are associated with the material’s composition and microstructure. The ac conductivity (σ_{ac}) is calculated through the relation: $\sigma_{ac} = \epsilon' \epsilon_0 \omega \tan \delta$, where ϵ' , ϵ_0 , ω and $\tan \delta$ denote the real part of dielectric permittivity, free space permittivity, angular frequency and tangent loss factor, respectively. The temperature dependence of ac conductivity for BTO and BSTMO has been

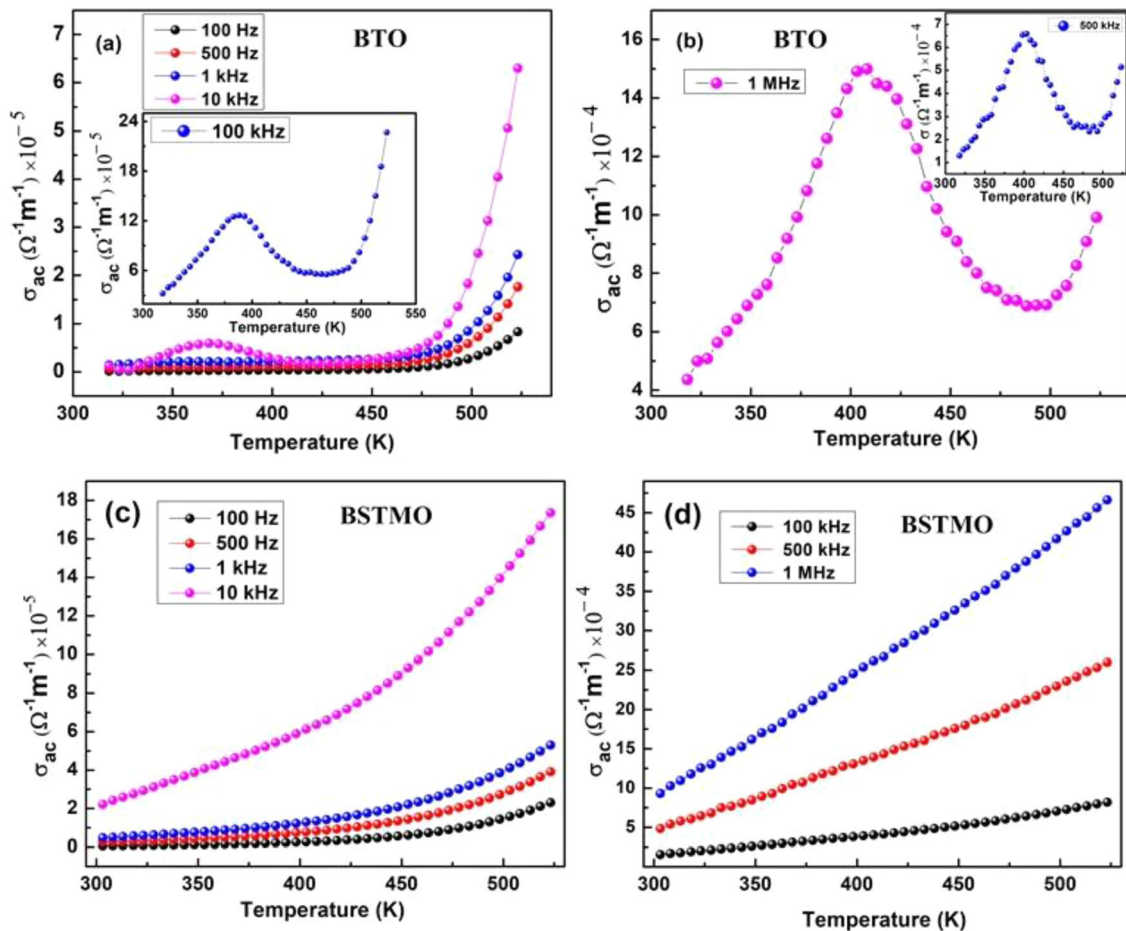


Fig. 12 Plots of σ_{ac} as a function of temperature at selected frequencies for **a b** BTO and **c d** BSTMO

investigated as shown in Fig. 12. It can be seen from the figure that the ac conductivity of the samples is enhanced with the rise in temperature. This increase may be ascribed to the augmented drift mobility and polaron hopping instigated due to thermal agitation. This effect is more prominent in the higher temperature range, where increased hopping of charge carriers contribute towards an increase in conductivity. Moreover, for lower frequencies (Fig. 12a, c), the electric field does not have much impact on the mobility of charges, hence the values of electrical conductivity is similar to σ_{dc} . But for higher frequencies, (Fig. 12b, d) the conductivity rises in accordance with the Jonscher's universal power law stated as $\sigma = A\omega^s$, where σ is the total conductivity, A is a constant, ω is the angular frequency and ' s ' is a frequency dependent parameter lying between 0 and 1 for ac conductivity. The higher values of the electrical conductivity may be attributed to the greater losses instigated in the material and also due to the creation of oxygen vacancies on account of doping.

In order to gain an insight into the conduction mechanism occurring in these materials, $\log\sigma_{ac}$ has been plotted against $\log\omega$ at different temperatures as shown in Fig. 13. The slope of these plots gives the value of the exponent ' s '. There are various theoretical models [56] which assist in comprehending the relaxations and electric transport mechanism by correlating ' s ' parameter with the temperature, such as correlated barrier hopping (CBH), non-overlapping small polaron tunnelling (NSPT), quantum mechanical tunnelling (QMT) and overlapping large polaron tunnelling (OLPT) models. The correlated barrier hopping (CBH) model presides over when the exponent ' s ' decreases with temperature, whereas NSPT model contributes when ' s ' value increases with rising temperature. The OLPT model dominates if the exponent ' s ' initially decreases followed by an increase, whereas the QMT model governs when ' s ' parameter is independent of temperature. It is observed from Fig. 13a, b that the value of ' s ', as determined at selected temperatures, lies in the range

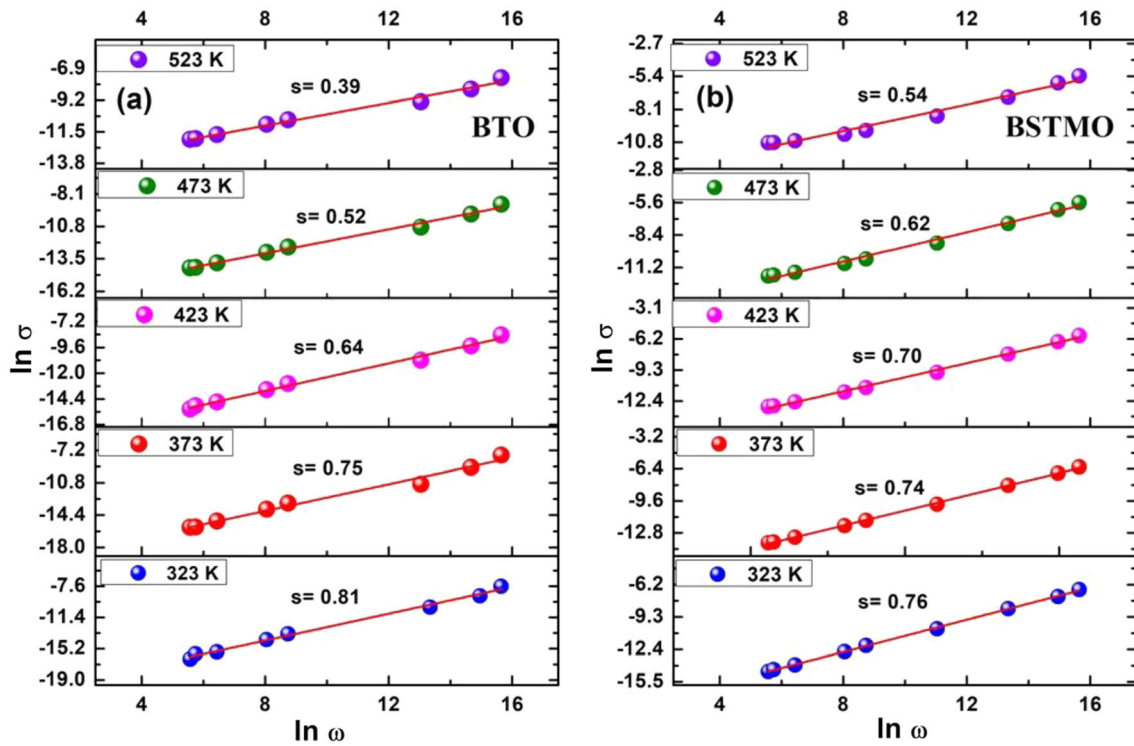


Fig. 13 Plots of $\ln \sigma_{ac}$ versus $\ln \omega$ at selected temperatures for **a** BTO and **b** BSTMO samples

of 0.39 to 0.81 for BTO and between 0.54 and 0.76 for BSTMO samples, respectively. The exponent ‘s’ exhibits a decrease with the increase in temperature for both the samples, which is in accordance with the correlated barrier hopping (CBH) conduction mechanism (Fig. 14a). CBH is the classical model which states that thermally activated charge carriers hop over the potential barrier between different lattice sites, upon temperature increase. The small grain size

of the samples might be the contributing factor for the dominance of this mechanism. The decrease in ‘s’ parameter is related to the enhanced mobility of free charge carriers via the localized energy states generated at the oxygen vacancy sites.

The exponent ‘s’ has been used to estimate the polaron binding energy (W_m) [56], also known as polaron hopping energy, for these systems. It is the amount of energy required for the polaron to hop

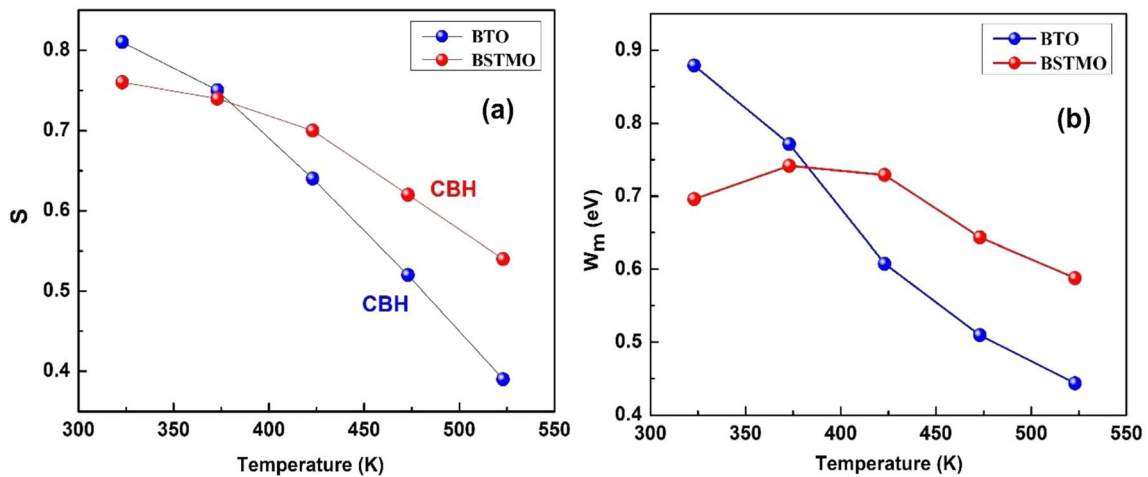


Fig. 14 Temperature dependent plots of **a** Exponent ‘s’, and **b** Binding energies for BTO and BSTMO samples

from one site to another. According to the CBH model, the polaron binding energy is given by

$$W_m = \frac{6k_B T}{(1-s)} \quad (16)$$

where, k_B is Boltzmann's constant. The variation of binding energy with temperature is given in Fig. 14b. The binding energy decreases with temperature for the BTO sample, indicating an increase in the number of hopping charge carriers, and ease in the motion of the polarons across the lattice sites. For the doped samples, initially, the binding energy increases slightly upon temperature increase but decreases afterward. This slight increase may be due to the incorporation of Mn ions that accumulates near the grain boundaries and results in grain growth suppression. This creates a potential barrier near the grain boundaries, hence making it difficult for the charge carriers to move [57, 58]. The barrier gets broken with the rise in temperature and hence we witness lower values of binding energy at higher temperatures.

The ac conductivity activation energy has been estimated using the Arrhenius law, given by,

$$\sigma = \sigma_0 e^{-\left(\frac{E_a}{k_B T}\right)} \quad (17)$$

where σ_0 is a pre-exponential term, k_B is the Boltzmann constant (8.61×10^{-5} eV/K), T is the absolute temperature and E_a represents the activation energy. Figure 15 shows the variation of $\ln\sigma$ with the inverse of temperature at 1 kHz and 100 kHz frequencies for BTO (Fig. 15a, b) and BSTMO (Fig. 15c, d) samples, respectively. The slopes obtained from the linear fit of these plots are utilized to estimate the activation energies at 1 kHz and 100 kHz. At 1 kHz frequency, in the lower temperature regime (300–400 K), activation energy lies around 0.09 eV, indicating that the conduction is due to polaronic hopping. The activation energy increases with the increase in temperature, which may be attributed to the hopping of oxygen vacancies within the TiO_6 octahedron and the flow of doubly ionized oxygen vacancies. Correspondingly, for 100 kHz (Fig. 15b, d), the values of activation energy escalate owing to increased ac conductivity, confirming that activation energy is frequency dependent.

Hence, the ac conductivity obeys Jonscher's universal power law, and the power factor 's' has been obtained upon fitting the data. The factor 's'

decreases with the rise in temperature, which is in accordance with the correlated barrier hopping (CBH) conduction mechanism. Moreover, the activation energy is enhanced upon the rise in temperature due to the charge hopping between localized states, and the transport mechanism transforms from electronic to ionic conduction.

3.6.1 Electrical dc resistivity transport analysis

The temperature dependence of dc resistivity is measured to study the effect of doping on the activation energy of the samples under study. The dc resistivity versus temperature plots for BTO and BSTMO samples are shown in Fig. 16. It is apparent from these plots that both the samples manifest a similar tendency of decrease in resistivity with the increase in temperature. This rapid reduction in resistivity, with the rise in temperature reveals that the samples are semiconducting in nature. Moreover, the increase in conductivity with increasing temperature (Inset: Fig. 16) depicts that as the temperature rises, more number of charge carriers are able to overcome the potential barrier and hop to the conduction band from the valence band. It can be inferred from the graphs that both the samples exhibit a negative temperature coefficient of resistivity (NTCR) [2] within the analyzed temperature range.

The value of resistivity is found to be $6.4 \times 10^8 \Omega\text{-m}$ for BTO at 310 K, which further reduces to $0.91 \times 10^7 \Omega\text{-m}$ at 470 K. However, for the doped sample, the resistivity is found to drop from $4.98 \times 10^7 \Omega\text{-m}$ to $2.36 \times 10^5 \Omega\text{-m}$, when the temperature is raised from 310 to 470 K. The resistivity data of the BTO and BSTMO samples have been listed in Table 5.

It is evident from Table 5 that the resistivity of (Sr, Mn) co-doped BTO is much lower than that of pristine BaTiO_3 . This is due to the Sr^{2+} content which influences the morphology of BaTiO_3 , hence affecting the grain-boundary conduction phenomena. The grain boundary permittivity decreases with the rise in temperature, in accordance with the Curie-Weiss law [23]. The associated potential barrier increases, thus slowing down the fall in the resistivity, leading to its almost constant value. Moreover, the reduction in the electrical resistivity is widely associated with the inability of the doped sample to achieve sufficient crystallization, which is evident from the microstructure analysis of the powders.

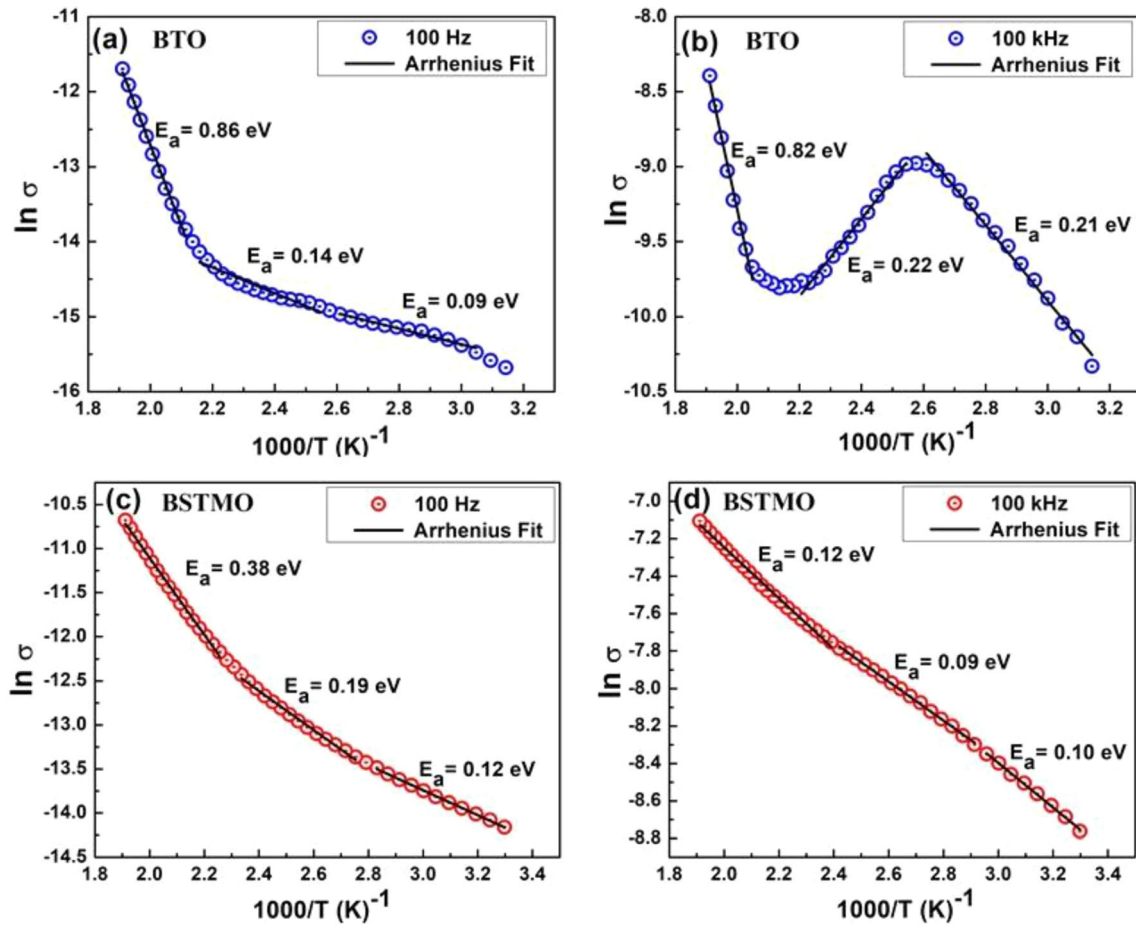


Fig. 15 a–d Variation of $\ln \sigma$ with inverse of temperature at selected frequencies for BTO and BSTMO samples

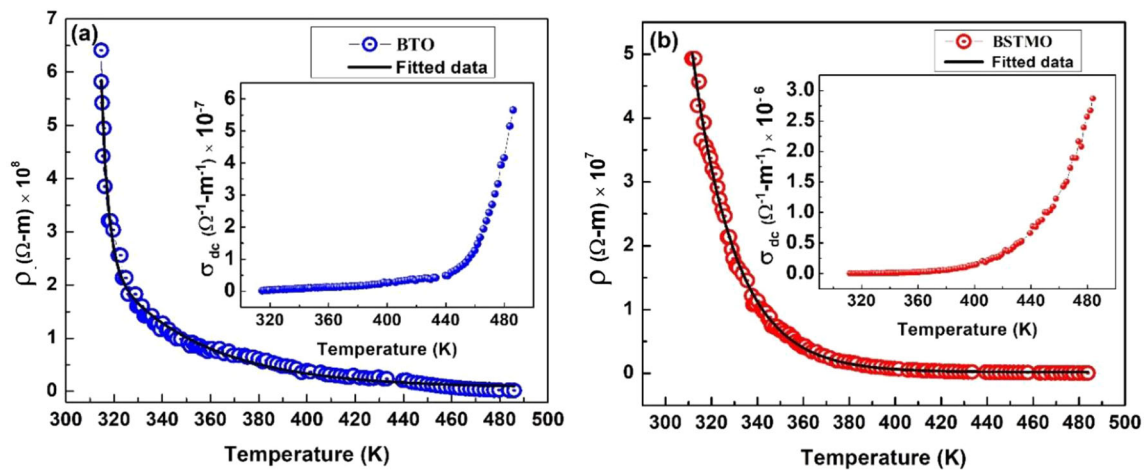


Fig. 16 Plots of resistivity against temperature for a BTO and b BSTMO samples along with fitted data. Insets show conductivity vs temperature plots for the same

The temperature at which the materials undergo transition from ferroelectric to paraelectric phase is largely dominated by the characteristics of the

dopants. The incorporation of Sr and Mn influences the grain boundaries and making them electrically homogenous. In particular, for the BSTMO sample,

Table 5 Resistivity of BTO and BSTMO samples at different values of temperatures

| Samples | Temperature (K) → | 310 | 330 | 350 | 370 | 390 | 410 | 430 | 450 | 470 |
|---------|-------------------------------------|------|------|------|------|------|------|------|------|------|
| BTO | $\rho(\Omega\text{-m}) \times 10^7$ | 64 | 15 | 10.3 | 6.43 | 4.12 | 2.34 | 1.99 | 1.62 | 0.91 |
| BSTMO | | 4.98 | 1.92 | 0.58 | 0.23 | 0.09 | 0.06 | 0.03 | 0.03 | 0.02 |

the Curie temperature shifts slightly towards the lower temperature. This shift is in close agreement with the previous reports [20, 32, 55]. The BaTiO₃ sample shows a transition from tetragonal phase to cubic phase at around 403 K (Fig. 16a), whereas the BSTMO samples undergo the phase transition near 390 K (Fig. 16b). The plot obtained upon studying the variation of resistivity with temperature of the samples was fitted and is shown in Fig. 16. The experimental data are found to converge with the best possible R² values, when fitted with the double exponential decay curve. The mathematical expression

$$y = y_0 + A_1 e^{-\frac{x-x_0}{t_1}} + A_2 e^{-\frac{x-x_0}{t_2}} \quad (18)$$

was derived upon fitting the curve and the obtained values of R² are 0.987 and 0.991 for BTO and BSTMO samples, respectively. The closeness of the R² values to unity is evident from the plot, where the fitting almost overlaps the experimental data. Hence, we obtained the mathematical relation for the dependency of resistivity upon temperature, which is given by Eq. (19).

$$\rho = \rho_0 + A_1 e^{\frac{T-x_0}{t_1}} + A_2 e^{\frac{T-x_0}{t_2}} \quad (19)$$

where ρ represents the resistivity, T stands for the temperature and $y_0, x_0, A_1, t_1, A_2, t_2$ are the fitting parameters whose estimated values have been tabulated in Table 6.

3.6.2 DC conductivity

The conductivity of the samples has been evaluated from the resistance data using the Eq. (20)

$$\sigma = \frac{t}{R \times A} \quad (20)$$

Table 6 Fitting parameters for resistivity vs temperature curves for BTO and BSTMO samples

| Samples | Parameters | | | | | | |
|---------|------------------------|-----------------|-------------------|-----------------|--------------------|-----------------|----------------|
| | $y_0(\Omega\text{-m})$ | $x_0(\text{K})$ | A_1 | $t_1(\text{K})$ | A_2 | $t_2(\text{K})$ | R ² |
| BTO | 6.9×10^6 | 313.27 | 5.5×10^8 | 2.94 | 2.40×10^8 | 39.29 | 0.987 |
| BSTMO | 1.7×10^5 | 311.75 | 2.4×10^7 | 18.79 | 2.48×10^7 | 18.79 | 0.991 |

where t and A represent the pellet thickness and cross-section area, respectively, and R stands for the experimentally measured resistance. The activation energy has been calculated through the Arrhenius law (Eq. 17).

Figure 17 depicts the variation of $\ln \sigma_{dc}$ with the inverse of temperature for BTO and BSTMO specimens. The experimental data have been fitted with the Arrhenius law to estimate the activation energy of the material. The values of activation energy as determined using the slope of $\ln \sigma$ vs $1/T$ plot are found to be 1.02 eV and 0.61 eV for the pristine and doped samples, respectively. The lowering of the activation energy in case of the Sr and Mn consolidated sample can be understood by the charge imbalance created due to the occupation of Mn²⁺ ion at the Ti⁴⁺ site. The difference in the oxidation states promotes the hopping of electrons in the TiO₆ octahedron, consequently reducing the E_a value. The doubly ionised oxygen vacancies contribute to the values of activation energy in the high temperature range [19, 59].

Therefore, it can be concluded that the electronic conduction mechanism dominates in the low temperature region whereas for higher temperatures, the electrical conduction is ionic in nature. Moreover, the gradual decrease in the resistivity of the sample with the increase in the temperature, highlight towards a semiconductor behaviour of the sample, with negative temperature coefficient of resistivity characteristics.

3.7 Ferroelectric properties

Figure 18 shows the room temperature polarization–electric field (P-E) hysteresis loops for BTO and

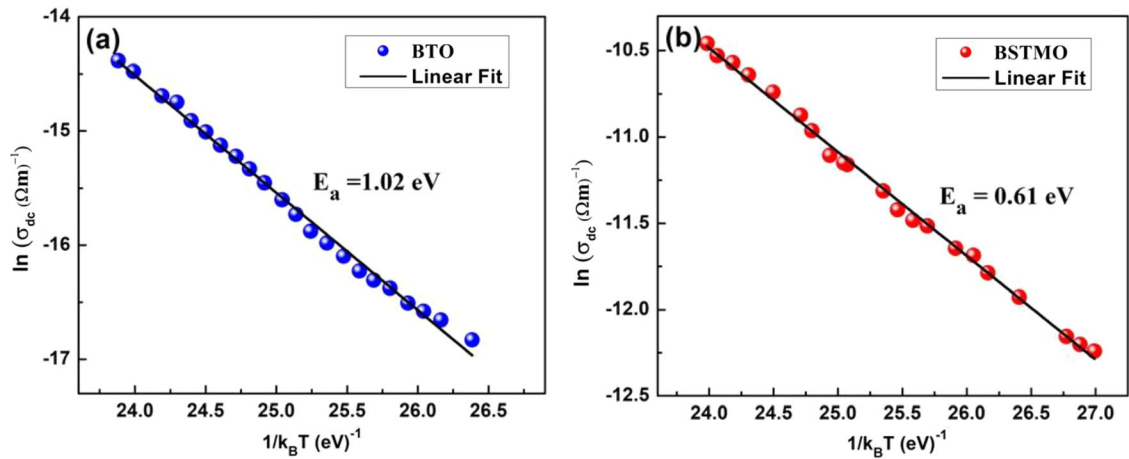


Fig. 17 Variation of $\ln \sigma_{dc}$ with inverse of temperature for a BTO and b BSTMO samples

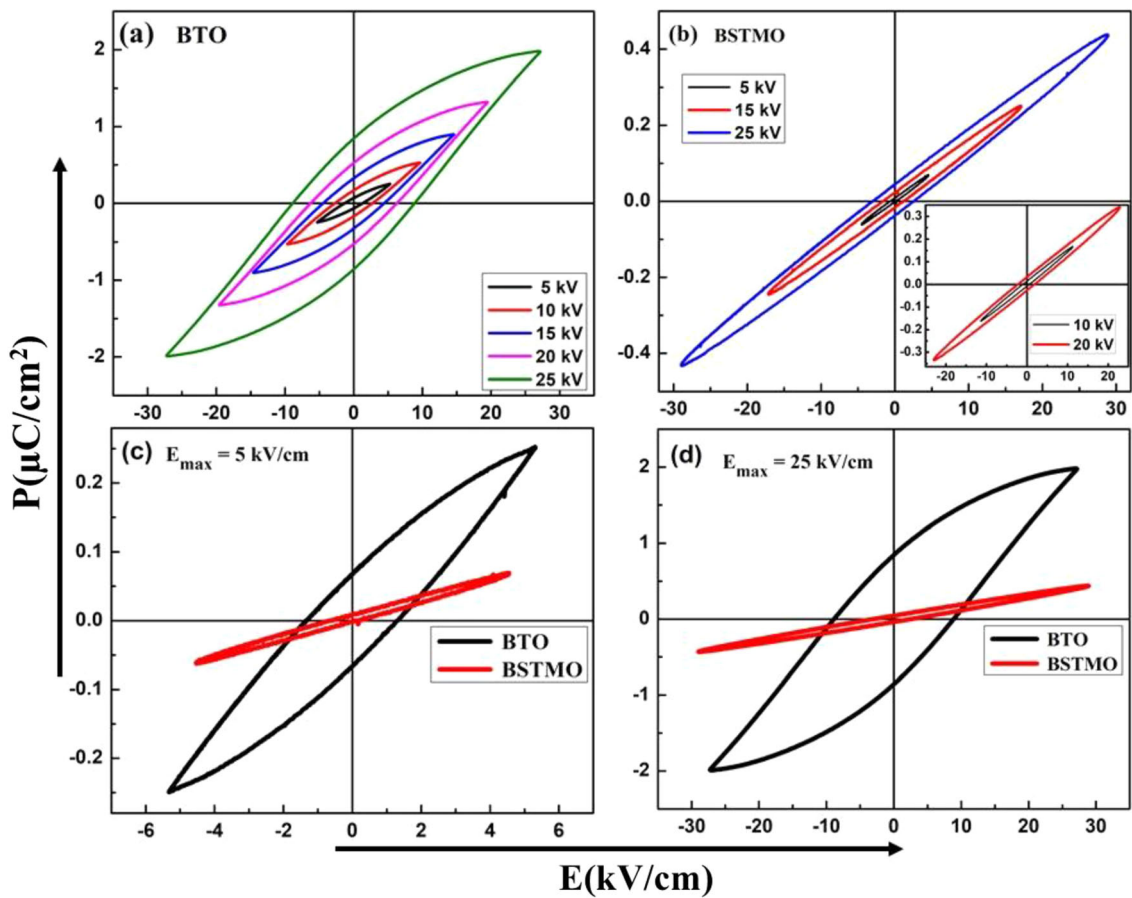


Fig. 18 a–d Ferroelectric hysteresis (P-E) loops for BTO and BSTMO samples

BSTMO ceramics at distinct applied electric fields ($E = 5, 10, 15, 20, 25$ kV/cm). The hysteresis data have been recorded at a frequency of 50 Hz with 100 nf internal capacitance and 100 kΩ resistance. BaTiO₃ displays spontaneous polarisation in its tetragonal

phase as evident from the P-E loops. The nonlinear trajectory of the P-E plot reveals the presence of ferroelectric polarization in the samples which does not achieve complete saturation, despite higher values of applied electric field. The applied electric field and

Table 7 Estimated values of maximum polarization (P_m), remnant polarization (P_r) and coercive field (E_c) of BTO and BSTMO ceramics at different values of applied electric field

| Samples | Applied electric field, E (kV/cm) | Maximum polarization P_{max} ($\mu\text{C}/\text{cm}^2$) | Remnant polarization P_r ($\mu\text{C}/\text{cm}^2$) | Coercive field E_c (kV/cm) |
|---------|-----------------------------------|--|--|------------------------------|
| BTO | 5 | 0.252 | 0.0299 | 1.3223 |
| | 10 | 0.536 | 0.169 | 2.755 |
| | 15 | 0.894 | 0.331 | 4.357 |
| | 20 | 1.316 | 0.532 | 6.295 |
| | 25 | 1.959 | 0.859 | 8.995 |
| BSTMO | 5 | 0.068 | 0.005 | 0.409 |
| | 10 | 0.164 | 0.011 | 0.844 |
| | 15 | 0.248 | 0.020 | 1.388 |
| | 20 | 0.338 | 0.029 | 2.026 |
| | 25 | 0.436 | 0.041 | 2.818 |

the nature of the dopants are the governing parameters for the values of the remnant polarization (P_r), maximum polarization (P_m), coercive field (E_c) and the loop contour. A detailed explanation is given below.

3.7.1 Impact of applied electric field on polarization parameters

At room temperature, BaTiO_3 exists in tetragonal symmetry with $P4mm$ space group, which is non-centrosymmetric in nature [60]. The positively charged Ti^{4+} ions occupy the centre while the faces are occupied by the negatively charged oxygen (O^{2-}) ions, i.e., centre of Ti^{4+} ions does not coincide with the negatively charged O^{2-} ions. When the external electric field interacts with the dielectric ceramic, these cationic and anionic charge centres are attracted towards the oppositely charged electrodes, forming a dipole. The distance between the charge centres increases with the applied field, ultimately increasing the dipole moment ($\mu = \sum qd$) and hence strengthening the net ionic polarisation ($P = \mu/V$). Additionally, as the force ($F = qE$) applied to the ferroelectric domain escalates, more number of electric dipoles align themselves in its direction, gradually raising the P_r and P_{max} values. The loops in Fig. 18 exhibits a strong dependence upon the applied electric field. The ferroelectric coercive field has been evaluated by $E_c = (E_{c+} + E_{c-})/2$ and the remnant polarization P_r by $(P_{r+} + P_{r-})/2$. The obtained values of E_c and P_r for selected values of applied electric field for BTO and BSTMO samples

have been tabulated in Table 7. In BTO, for a field of 5 kV, the P_r and P_{max} values are $0.0299 \mu\text{C}/\text{cm}^2$ and $0.2515 \mu\text{C}/\text{cm}^2$, respectively. These values enhanced to $0.8593 \mu\text{C}/\text{cm}^2$ and $1.9586 \mu\text{C}/\text{cm}^2$, respectively, for 25 kV field. A similar trend is obtained for the doped sample, too. The area of the loop has been found to increase with the rise in the electric field for both the samples, which may be attributed to increased mobile charge carriers leading to leakage current.

3.7.2 Dependency of polarization parameters on grain size

A well-behaved hysteresis loop is observed for pristine BTO, however, the doped sample exhibits almost linear ferroelectric hysteresis with reduced P_r and E_c . A suppression in the ferroelectricity is observed along with the gradual emergence of a paraelectric behaviour which leads to a sudden drop in the polarization parameters. It may be due to the creation of oxygen vacancies in the sample under the effect of Mn doping at the Ti site. The decreased polarization in BSTMO can also be explained on the basis of the obtained structural data. The shift of the tolerance factor towards $\tau = 1$, indicates that (Sr, Mn) inclusion promotes a more symmetric structure, i.e., the system is going toward the cubic phase, which does not favour ferroelectricity, which can also be verified from the increase in the Ti–O–Ti bond angle for the doped sample. This reduction in non-centrosymmetry is due to the suppression of the tetragonal state and ultimately reduces the ferroelectricity within the

doped sample leading to the linear polarisation response. For a particular applied field, $E = 15 \text{ kV/cm}$, the maximum polarization (P_m) is observed to be $0.89 \mu\text{C/cm}^2$ for BaTiO_3 and it reduces down to $0.24 \mu\text{C/cm}^2$ for (Sr, Mn) co-doped sample. The large grain sizes direct the electric domain orientation under the applied electric field and impart good ferroelectric behaviour as in case of pristine sample which has an average grain size of $1.05 \mu\text{m}$ [61]. With the reduction in grain size, the potential barriers in the domains increase accompanied by a redistribution of point defects and space charge at grain boundaries, that consequently reduces the ferroelectric nature of the material [12]. Venkata et al. [54] have reported that the large grain size of material overcame the energy barrier, leading to the easier reversal of ferroelectric domains. Tan et al. [62] have reported that the ferroelectric nature of BaTiO_3 ceramics first increases with the decrease in average grain size, and reaches a maximum value in the grain size range of $0.8\text{--}1.1 \mu\text{m}$. Afterwards, it rapidly decreases with further decrease of grain size. The obtained results of BTO and BSTMO samples are consistent with the reported trend. The lower values of the grain size significantly impact the nature of P-E loops.

Hence, a reduction in non-centrosymmetry is observed in the (Sr, Mn) co-doped sample which is attributed to the suppression of the tetragonal phase. This ultimately reduces the ferroelectricity within the doped sample leading to the linear polarisation response, which corresponds to the paraelectric state of the sample.

4 Conclusion

Lead-free ferroelectric, crystalline samples of $\text{Ba}_{1-x}\text{Sr}_x\text{Ti}_{1-x}\text{Mn}_x\text{O}_3$ at $x = (0.0, 0.1)$ have been successfully synthesized by the solid-state reaction route and their structural, dielectric, ferroelectric and electrical transport properties have been studied using various analytical techniques. XRD patterns revealed tetragonal phase ($P4mm$) for each sample. Ultrasonication of the samples prior to grinding promoted the formation of small grains with uniform microstructure. It might also be responsible for producing monophasic crystalline samples at a relatively lower sintering temperature of $900 \text{ }^\circ\text{C}$. Rietveld refinement analysis confirmed that the lattice parameters, bond

lengths, and bond angles are significantly influenced upon doping. The crystallite size is estimated using Scherrer equation and Williamson-Hall approach and it is found to decrease with doping. FTIR analysis reveals absorptions bands in the region of $520\text{--}560 \text{ cm}^{-1}$ and $425\text{--}435 \text{ cm}^{-1}$ corresponding to Ti–O stretching (ν_1) and bending vibrations (ν_2), respectively, confirming the formation of TiO_6 octahedron. SEM micrographs reveal that the grain size lies in the range $0.2\text{--}1.4 \mu\text{m}$. The average grain size decreases from $1.05 \mu\text{m}$ for BTO to $0.68 \mu\text{m}$ for the doped sample. The dielectric constant and loss tangent reduce with the increase in frequency as well as with co-doping. The samples exhibit universal dielectric response (UDR) phenomena for the frequency range of $42 \text{ Hz}\text{--}50 \text{ kHz}$. The temperature dependent dielectric permittivity exhibits a thermally activated relaxation peak near 400 K in the BTO sample which shifts towards lower temperatures for the doped sample, indicating a decrease in the Curie temperature. The conduction mechanism is governed by the correlated barrier hopping (CBH) model for both the samples. The ac conductivity data have been used to estimate the binding energies (W_m) of the polarons and activation energy at different temperatures. Ferroelectric studies demonstrate that the pristine BaTiO_3 favours the ferroelectricity, affirming a non-centrosymmetric nature of the BaTiO_3 but for the co-doped sample, there is decrement in all ferroelectric variables indicating the emergence of centrosymmetry in the crystal structure.

Acknowledgements

Mehroosh Fatema is grateful to DST, Government of India for financial support under the INSPIRE Fellowship Program (DST/INSPIRE Fellowship/2017/IF170728). Authors are also thankful to Dr. Naseem Ahmad, Department of Applied Physics for dielectric measurements and to USIF, AMU, Aligarh for SEM facilities.

Author contributions

Sample preparation, data collection and analysis, writing—original draft preparation: MF, data collection and analysis: AB, AS, SM, MA, NZ and AAAQ,

review and editing: WK, conceptualization, review and editing: SH.

Funding

Funding was provided by Department of Science and Technology, Government of India, India (DST/INSPIRE Fellowship/2017/IF170728).

Data availability

Data will be made available by the corresponding author on reasonable request.

Declarations

Conflict of interest The authors have no competing interests to declare that are relevant to the content of this article.

Ethical approval This manuscript is the authors' own original work, which has not been previously published elsewhere. All sources used are properly disclosed and all authors have personally and actively involved in substantial work leading to this paper.

References

1. Q. Liu, J. Liu, D. Lu, W. Zheng, C. Hu, Structural evolution and dielectric properties of Nd and Mn co-doped BaTiO₃ ceramics. *J. Alloys Compd.* **760**, 31–41 (2018). <https://doi.org/10.1016/j.jallcom.2018.05.089>
2. Y. Wang, Y. Pu, P. Zhang, Investigation of dielectric relaxation in BaTiO₃ ceramics modified with BiYO₃ by impedance spectroscopy. *J. Alloys Compd.* **653**, 596–603 (2015). <https://doi.org/10.1016/j.jallcom.2015.09.012>
3. W.S. Clabaugh, E.M. Swiggard, R. Gilchrist, Preparation of barium titanate tetrahydrate for conversion to barium titanate of high purity. *J. Res. Natl. Bur. Stand.* **56**(1956), 289 (1934). <https://doi.org/10.6028/jres.056.037>
4. L.M. Arunachalam, D. Chakravorty, E.C. Subbarao, Synthesis and properties of manganese-doped barium titanate. *Bull. Mater. Sci.* **9**, 159–168 (1987). <https://doi.org/10.1007/BF02744264>
5. L.M. Zivkovic, V.V. Paunovic, N.L. Stamenkov, M.M. Miljkovic, The effect of secondary abnormal grain growth on the dielectric properties of La/Mn Co-doped BaTiO₃ ceramics. *Sci. Sinter.* **38**, 273–281 (2006). <https://doi.org/10.2298/SOS0603273Z>
6. C.W. Nan, M.I. Bichurin, S. Dong, D. Viehland, G. Srinivasan, Multiferroic magnetoelectric composites: historical perspective, status, and future directions. *J. Appl. Phys.* (2008). <https://doi.org/10.1063/1.2836410>
7. H. Sun, S. Duan, X. Liu, D. Wang, H. Sui, Lead-free Ba_{0.98}Ca_{0.02}Zr_{0.02}Ti_{0.98}O₃ ceramics with enhanced electrical performance by modifying MnO₂ doping content and sintering temperature. *J. Alloys Compd.* **670**, 262–267 (2016). <https://doi.org/10.1016/j.jallcom.2016.02.008>
8. C.H. Perry, D.B. Hall, Temperature dependence of the Raman spectrum of BaTiO₃. *Phys. Rev. Lett.* **15**, 700–702 (1965). <https://doi.org/10.1103/PhysRevLett.15.700>
9. X. Jin, D. Sun, M. Zhang, Y. Zhu, J. Qian, Investigation on FTIR spectra of barium calcium titanate ceramics. *J. Electroceram.* **22**, 285–290 (2009). <https://doi.org/10.1007/s10832-007-9402-1>
10. Y.I. Yuzyuk, Raman scattering spectra of ceramics, films, and superlattices of ferroelectric perovskites: a review. *Phys. Solid State.* **54**, 1026–1059 (2012). <https://doi.org/10.1134/S1063783412050502>
11. A.J. Anthoniappen, C.S. Tu, P. Chen, Y.U. Idzerda, S. Chiu, Raman spectra and structural stability in B- site manganese doped ferroelectric ceramics. *J. Eur. Ceram. Soc.* **13**, 3495–3506 (2015). <https://doi.org/10.1016/j.jeurceramsoc.2015.05.002>
12. T. Zaman, M.K. Islam, M.A. Rahman, A. Hussain, M.A. Matin, M.S. Rahman, Mono and co-substitution of Sr²⁺ and Ca²⁺ on the structural, electrical and optical properties of barium titanate ceramics. *Ceram. Int.* **45**, 10154–10162 (2019). <https://doi.org/10.1016/j.ceramint.2019.02.064>
13. Y. Wang, M.K. Niranjan, K. Janicka, J.P. Velev, M.Y. Zhuravlev, S.S. Jaswal, E.Y. Tsybmal, Ferroelectric dead layer driven by a polar interface. *Phys. Rev. B* **82**, 1–10 (2010). <https://doi.org/10.1103/PhysRevB.82.094114>
14. M. Ganguly, S.K. Rout, T.P. Sinha, S.K. Sharma, H.Y. Park, C.W. Ahn, I.W. Kim, Characterization and rietveld refinement of a-site deficient lanthanum doped barium titanate. *J. Alloys Compd.* **579**, 473–484 (2013). <https://doi.org/10.1016/j.jallcom.2013.06.104>
15. M.D. Glinchuk, I.P. Bykov, S.M. Kornienko, V.V. Laguta, A.M. Slipenyuk, A.G. Bilous, O.I. V'yunov, O.Z. Yanchevskii, Influence of impurities on the properties of rare-earth-doped barium- titanate ceramics. *J. Mater. Chem.* **10**, 941–947 (2000)
16. F.A. Ismail, R.A.M. Osman, M.S. Idris, Review on dielectric properties of rare earth doped barium titanate. *AIP Conf. Proc.* (2016). <https://doi.org/10.1063/1.4958786>

17. J. Jeong, E.J. Lee, Y.H. Han, Electrical properties of holmium-doped BaTiO₃. *Jpn. J. Appl. Physics*. **44**, 4047–4051 (2005). <https://doi.org/10.1143/JJAP.44.4047>
18. A. Surampalli, I. Schiesaro, P. Corsi, C. Meneghini, V.G. Sathe, A. Sagdeo, A.K. Sinha, G. Aquilanti, E. Welter, V.R. Reddy, Evidence of structural modifications in the region around the broad dielectric maxima in the 30% Sn-doped barium titanate relaxor. *Phys. Rev. B*. **100**, 134104 (2019). <https://doi.org/10.1103/PhysRevB.100.134104>
19. M. Arshad, H. Du, M.S. Javed, A. Maqsood, I. Ashraf, S. Hussain, W. Ma, H. Ran, Fabrication, structure, and frequency-dependent electrical and dielectric properties of Sr-doped BaTiO₃ ceramics. *Ceram. Int.* **46**, 2238–2246 (2020). <https://doi.org/10.1016/j.ceramint.2019.09.208>
20. R.A.V. Ortíz, J. Muñoz-Saldaña, F.J. Espinoza-Beltrán, Mechano-synthesis and reactive sintering of Ba_{1-x}Sr_xTiO₃ ceramics. *Mater. Res. Innov.* **13**, 368–371 (2009). <https://doi.org/10.1179/143307509X441586>
21. M.B. Chamekh, Z.B. Achour, A. Thamri, R. Chtourou, E. Dhahri, O. Touayar, Structural and electrical characterization of strontium doped barium titanate for radiometric measurement. *Chem. Phys. Lett.* (2020). <https://doi.org/10.1016/j.cplett.2020.138008>
22. E. Duverger, B. Jannot, F.M. Michel-Calendini, M. Maglione, Manganese doping effects in BaTiO₃: Electronic structure E. P. R. and conductivity studies. *Ferroelectrics* **125**, 301–306 (1992). <https://doi.org/10.1080/00150199208017084>
23. V. Paunovic, V. Mitic, M. Marjanovic, L. Kocic, Dielectric properties of La/Mn codoped barium titanate ceramics. *Facta Univ.* **29**, 285–296 (2016). <https://doi.org/10.2298/fuee1602285p>
24. K. Madhan, R. Thiyagarajan, C. Jagadeeshwaran, A.P.B. Selvadurai, V. Pazhanivelu, K. Aravinth, W. Yang, R. Murugaraj, Investigations on the phase transition of Mn-doped BaTiO₃ multifunctional ferroelectric ceramics through Raman, dielectric, and magnetic studies. *J. Sol-Gel Sci. Technol.* **88**, 584–592 (2018). <https://doi.org/10.1007/s10971-018-4835-3>
25. Y. Zhu, C. Quan, Y. Ma, Q. Wang, W. Mao, X. Wang, J. Zhang, Y. Min, J. Yang, X. Li, W. Huang, Effect of Eu, Mn co-doping on structural, optical and magnetic properties of BiFeO₃ nanoparticles. *Mater. Sci. Semicond. Process.* **57**, 178–184 (2017). <https://doi.org/10.1016/j.mssp.2016.10.023>
26. N.T. Dang, D.P. Kozlenko, T.L. Phan, S.E. Kichanov, N.V. Dang, T.D. Thanh, L.H. Khiem, S.H. Jabarov, T.A. Tran, D.B. Vo, B.N. Savenko, Structural polymorphism of Mn-doped BaTiO₃. *J. Electron. Mater.* **45**, 2477–2483 (2016). <https://doi.org/10.1007/s11664-016-4382-z>
27. Z. Shen, X. Wang, H. Gong, L. Wu, L. Li, Effect of MnO₂ on the electrical and dielectric properties of Y-doped Ba_{0.95}Ca_{0.05}Ti_{0.85}Zr_{0.15}O₃ ceramics in reducing atmosphere. *Ceram. Int.* **40**, 13833–13839 (2014). <https://doi.org/10.1016/j.ceramint.2014.05.100>
28. M.C. Maldonado-Orozco, M.T. Ochoa-Lara, J.E. Sosa-Márquez, R.P. Talamantes-Soto, A. Hurtado-Macías, R.L. Antón, J.A. González, J.T. Holguín-Momaca, S.F. Olive-Méndez, F. Espinosa-Magaña, Absence of ferromagnetism in ferroelectric Mn-doped BaTiO₃ nanofibers. *J. Am. Ceram. Soc.* **102**, 2800–2809 (2019)
29. H.T. Langhammer, T. Müller, K.H. Felgner, H.P. Abicht, Influence of strontium on manganese-doped barium titanate ceramics. *Mater. Lett.* **42**, 21–24 (2000). [https://doi.org/10.1016/S0167-577X\(99\)00153-6](https://doi.org/10.1016/S0167-577X(99)00153-6)
30. R.M. Glaister, H.F. Kay, An investigation of the cubic-hexagonal transition in barium titanate. *Proc. Phys. Soc.* **76**, 763–771 (1960). <https://doi.org/10.1088/0370-1328/76/5/317>
31. A.I. Lebedev, I.A. Sluchinskaya, On the nature of change in Ni oxidation state in BaTiO₃–SrTiO₃ system. *Ferroelectrics* **501**, 1–8 (2016). <https://doi.org/10.1080/00150193.2016.1198196>
32. M.B. Chamekh, Z.B. Achour, A. Thamri, R. Chtourou, E. Dhahri, O. Touayar, Structural and electrical characterization of strontium doped barium titanate for radiometric measurement. *Chem. Phys. Lett.* **761**, 138008 (2020). <https://doi.org/10.1016/j.cplett.2020.138008>
33. A. Semenov, A. Dedyk, I. Mylnikov, O. Pakhomov, A. Es'kov, A. Anokhin, V. Krylov, A. Burovikhin, Y. Pavlova, A. Tselev, A. Kholkin, Mn-doped BaTiO₃ ceramics: thermal and electrical properties for multicaloric applications. *Materials (Basel)*. **12** (2019) 1–9. <https://doi.org/10.3390/ma12213592>
34. N. Koshy, D.N. Singh, B. Jha, S. Kadali, J. Patil, Characterization of Na and Ca zeolites synthesized by various hydrothermal treatments of fly ash. *Adv. Civ. Eng. Mater.* **4**, 131–143 (2015). <https://doi.org/10.1520/ACEM20140048>
35. K. Momma, F. Izumi, VESTA: a three-dimensional visualization system for electronic and structural analysis. *J. Appl. Crystallogr.* **41**, 653–658 (2008). <https://doi.org/10.1107/S0021889808012016>
36. I. Calisir, D.A. Hall, Chemical heterogeneity and approaches to its control in BiFeO₃–BaTiO₃ lead-free ferroelectrics. *J. Mater. Chem. C*. **6**, 134–146 (2017). <https://doi.org/10.1039/c7tc04122e>
37. T. Sato, S. Takagi, S. Deledda, B.C. Hauback, S.I. Orimo, Extending the applicability of the Goldschmidt tolerance

- factor to arbitrary ionic compounds. *Sci. Rep.* **6**, 1–10 (2016). <https://doi.org/10.1038/srep23592>
38. C.M. Culbertson, A.T. Flak, M. Yatskin, P.H.Y. Cheong, D.P. Cann, M.R. Dolgos, Neutron total scattering studies of group II titanates (ATiO_3 , $A^{2+} = \text{Mg, Ca, Sr, Ba}$). *Sci. Rep.* **10**, 1–10 (2020). <https://doi.org/10.1038/s41598-020-60475-8>
 39. A.L. Patterson, The scherrer formula for X-ray particle size determination. *Phys. Rev.* **56**, 978–982 (1939). <https://doi.org/10.1103/PhysRev.56.978>
 40. R.G. Egdell, E. Bruton, Henry moseley. X-ray spectroscopy and the periodic table (2020). <https://doi.org/10.1098/rsta.2019.0302rsta20190302>
 41. G.K. Williamson, W.H. Hall, X-ray line broadening from filed aluminium and wolfram. *Acta Metall.* **1**, 22–31 (1953). [https://doi.org/10.1016/0001-6160\(53\)90006-6](https://doi.org/10.1016/0001-6160(53)90006-6)
 42. V. Biju, N. Sugathan, V. Vrinda, S.L. Salini, Estimation of lattice strain in nanocrystalline silver from X-ray diffraction line broadening. *J. Mater. Sci.* **43**, 1175–1179 (2008). <https://doi.org/10.1007/s10853-007-2300-8>
 43. W. Zhang, Q. Feng, E. Hosono, D. Asakura, J. Miyawaki, Y. Harada, Tetragonal distortion of a $\text{BaTiO}_3/\text{Bi}_{0.5}\text{Na}_{0.5}\text{TiO}_3$ nanocomposite responsible for anomalous piezoelectric and ferroelectric behaviors. *ACS Omega* **5** (2020) 22800–22807. <https://doi.org/10.1021/acsomega.0c01845>.
 44. Y. Rosenberg, V.S. Machavariani, A. Voronel, S. Garber, A. Rubshtein, A.I. Frenkel, E.A. Stern, Strain energy density in the X-ray powder diffraction from mixed crystals and alloys. *J. Phys. Condens. Matter.* **12**, 8081–8088 (2000). <https://doi.org/10.1088/0953-8984/12/37/307>
 45. A. Alqahtani, S. Husain, A. Somvanshi, W. Khan, Structural, morphological, thermal and optical investigations on Mn doped GdCrO_3 . *J. Alloys Compd.* **804**, 401–414 (2019). <https://doi.org/10.1016/j.jallcom.2019.07.028>
 46. R.T. Mara, G.B.B.M. Sutherland, H.V. Tyrell, Infrared spectrum of barium titanate [5]. *Phys. Rev.* **96**, 801–802 (1954). <https://doi.org/10.1103/PhysRev.96.801>
 47. C.H. Perry, B.N. Khanna, G. Rupprecht, Infrared studies of perovskite titanates. *Phys. Rev.* **135**, 1–5 (1964). <https://doi.org/10.1103/PhysRev.135.A408>
 48. R. Ashiri, Detailed FT-IR spectroscopy characterization and thermal analysis of synthesis of barium titanate nanoscale particles through a newly developed process. *Vib. Spectrosc.* **66**, 24–29 (2013). <https://doi.org/10.1016/j.vibspec.2013.02.001>
 49. A. Somvanshi, A. Ahmad, S. Husain, S. Manzoor, A.A.A. Qahtan, N. Zarrin, M. Fatema, W. Khan, Structural modifications and enhanced ferroelectric nature of $\text{NdFeO}_3\text{-PbTiO}_3$ composites. *Appl. Phys. A* **127** (2021). <https://doi.org/10.1007/s00339-021-04562-1>.
 50. R.A. El-Mallawany, Theoretical and experimental IR spectra of binary rare earth tellurite glasses-I. *Infrared Phys.* **29**, 781–785 (1989). [https://doi.org/10.1016/0020-0891\(89\)90125-5](https://doi.org/10.1016/0020-0891(89)90125-5)
 51. A. Sasmal, S. Sen, P.S. Devi, Significantly suppressed leakage current and reduced band gap of BiFeO_3 through Ba–Zr Co-Substitution: Structural, optical, electrical and magnetic study. *Mater. Chem. Phys.* **254**, 123362 (2020). <https://doi.org/10.1016/j.matchemphys.2020.123362>
 52. F. Dang, K. Kato, H. Imai, S. Wada, H. Haneda, M. Kuwabara, A new effect of ultrasonication on the formation of BaTiO_3 nanoparticles. *Ultrason. Sonochem.* **17**, 310–314 (2010). <https://doi.org/10.1016/j.ultsonch.2009.08.006>
 53. M. Desmond, N. Mavrogiannis, Z. Gagnon, Maxwell-Wagner polarization and frequency-dependent injection at aqueous electrical interfaces. *Phys. Rev. Lett.* **109**, 1–5 (2012). <https://doi.org/10.1103/PhysRevLett.109.187602>
 54. V.R. Mudinepalli, L. Feng, W.C. Lin, B.S. Murty, Effect of grain size on dielectric and ferroelectric properties of nanostructured $\text{Ba}_{0.8}\text{Sr}_{0.2}\text{TiO}_3$ ceramics, *J. Adv. Ceram.* **4** (2015) 46–53. <https://doi.org/10.1007/s40145-015-0130-8>.
 55. A. Kumari, B.D. Ghosh, Effect of strontium doping on structural and dielectric behaviour of barium titanate nanoceramics. *Adv. Appl. Ceram.* **117**, 427–435 (2018). <https://doi.org/10.1080/17436753.2018.1491166>
 56. A.A.A. Qahtan, S. Husain, A. Somvanshi, W. Khan, Y.K. Manea, Influence of Mn doping on dielectric properties, conduction mechanism and photocatalytic nature of gadolinium-based orthochromites. *J. Mater. Sci. Mater. Electron.* **31**, 9335–9351 (2020). <https://doi.org/10.1007/s10854-020-03474-9>
 57. E. Brzozowski, M.S. Castro, Conduction mechanism of barium titanate ceramics. *Ceram. Int.* **26**, 265–269 (2000). [https://doi.org/10.1016/S0272-8842\(99\)00052-8](https://doi.org/10.1016/S0272-8842(99)00052-8)
 58. M.A. Zubair, C. Leach, Modeling the resistance-temperature characteristic of a positive temperature coefficient thermistor, using experimentally determined permittivity data. *Appl. Phys. Lett.* **91**, 89–92 (2007). <https://doi.org/10.1063/1.2768034>
 59. N. Sareecha, W.A. Shah, A. Maqsood, M. Anis-ur-Rehman, M. L. Mirza, Fabrication and electrical investigations of Pb-doped BaTiO_3 ceramics. *Mater. Chem. Phys.* **193** (2017) 42–49. <https://doi.org/10.1016/j.matchemphys.2017.01.088>.
 60. S. Sanna, C. Thierfelder, S. Wippermann, T.P. Sinha, W.G. Schmidt, Barium titanate ground- and excited-state properties from first-principles calculations. *Phys. Rev. B* **83**, 1–9 (2011). <https://doi.org/10.1103/PhysRevB.83.054112>
 61. W. Eerenstein, N.D. Mathur, J.F. Scott, Multiferroic and magnetoelectric heterostructures. *Nature* **442**, 759–765 (2006). <https://doi.org/10.1016/j.actamat.2011.12.024>

62. Y. Tan, J. Zhang, Y. Wu, C. Wang, V. Koval, B. Shi, H. Ye, R. McKinnon, G. Viola, H. Yan, Unfolding grain size effects in barium titanate ferroelectric ceramics. *Sci. Rep.* **5**, 15–21 (2015). <https://doi.org/10.1038/srep09953>

Publisher's Note Springer Nature remains neutral with regard to jurisdictional claims in published maps and institutional affiliations.